

## BROAD H $\beta$ EMISSION-LINE VARIABILITY IN A SAMPLE OF 102 LOCAL ACTIVE GALAXIES

JORDAN N. RUNCO<sup>1</sup>, MAREN COSENS<sup>1</sup>, VARDHA N. BENNERT<sup>1</sup>, BRYAN SCOTT<sup>1</sup>, S. KOMOSSA<sup>2</sup>, MATTHEW A. MALKAN<sup>3</sup>, MARIANA S. LAZAROVA<sup>4</sup>, MATTHEW W. AUGER<sup>5</sup>, TOMMASO TREU<sup>3</sup>, DAESEONG PARK<sup>6</sup>

<sup>1</sup>Physics Department, California Polytechnic State University, San Luis Obispo CA 93407, USA; jrunco@calpoly.edu, mcosens@calpoly.edu, vbennert@calpoly.edu

<sup>2</sup>Max-Planck-Institut für Radioastronomie, Auf dem Hügel 69, 53121, Bonn, Germany

<sup>3</sup>Department of Physics, University of California, Los Angeles, CA 90095, USA; malkan@astro.ucla.edu, tt@physics.ucla.edu

<sup>4</sup>Department of Physics and Physical Science, University of Nebraska Kearney, Kearney, NE 68849; lazarovam2@unk.edu

<sup>5</sup>Institute of Astronomy, Madingley Road, Cambridge CB3 0HA, UK; mauger@ast.cam.ac.uk and

<sup>6</sup>Korea Astronomy and Space Science Institute, Daejeon, 34055, Republic of Korea; daeseongpark@kasi.re.kr

*Draft version August 28, 2018*

### ABSTRACT

A sample of 102 local ( $0.02 \leq z \leq 0.1$ ) Seyfert galaxies with black hole masses  $M_{\text{BH}} > 10^7 M_{\odot}$  was selected from the Sloan Digital Sky Survey (SDSS) and observed using the Keck 10-m telescope to study the scaling relations between  $M_{\text{BH}}$  and host galaxy properties. We study profile changes of the broad H $\beta$  emission line within the  $\sim 3$ –9 year time-frame between the two sets of spectra. The variability of the broad H $\beta$  emission line is of particular interest, not only since it is used to estimate  $M_{\text{BH}}$ , but also since its strength and width is used to classify Seyfert galaxies into different types. At least some form of broad-line variability (in either width or flux) is observed in the majority ( $\sim 66\%$ ) of the objects, resulting in a Seyfert-type change for  $\sim 38\%$  of the objects, likely driven by variable accretion and/or obscuration. The broad H $\beta$  line virtually disappears in 3/102 ( $\sim 3\%$ ) extreme cases. We discuss potential causes for these changing-look AGNs. While similar dramatic transitions have previously been reported in the literature, either on a case-by-case basis or in larger samples focusing on quasars at higher redshifts, our study provides statistical information on the frequency of H $\beta$  line variability in a sample of low-redshift Seyfert galaxies.

*Subject headings:* accretion, accretion disks – black hole physics – galaxies: active – galaxies: evolution – galaxies: Seyferts – galaxies: statistics

### 1. INTRODUCTION

Observed relations between the mass of the supermassive black hole ( $M_{\text{BH}}$ ) at the center of a galaxy and the properties of its host galaxy – such as host galaxy mass (Magorrian et al. 1998), luminosity (Kormendy & Richstone 1995), and stellar velocity dispersion (Ferrarese & Merritt 2000; Gebhardt et al. 2000) – imply a relationship between galaxy evolution and black hole (BH) growth (for a recent review see Kormendy & Ho 2013; Graham 2016, and references therein). In the local Universe,  $M_{\text{BH}}$  can be measured by spatially resolving the BH sphere of influence using stellar or gas kinematics (e.g., van der Marel et al. 1998; Gebhardt et al. 2000). At larger distances, the only way to estimate  $M_{\text{BH}}$  is by resolving the BH sphere of influence as it responds to variations in continuum in galaxies with an active galactic nucleus (AGN). In AGNs, the BH is actively growing via an accretion disk of infalling material. The high energy photons emitted by the hot accretion disk ionize the surrounding gas clouds, the broad-line region (BLR) in the vicinity of the BH, and the narrow-line region (NLR) further out. Reverberation mapping (Wandel et al. 1999; Kaspi et al. 2005; Bentz et al. 2013) traces variations in the accretion-disk continuum luminosity and the time-delayed response of the BLR flux to determine the size of the BLR, using light-travel time arguments. The velocity of the BLR gas can be determined from the Doppler broadening of the emission lines (such as the broad H $\beta$  line in the rest-frame optical). By assuming a dimensionless virial coefficient to describe the kinematics and geometry of the BLR, the velocity and size of the BLR combined yield  $M_{\text{BH}}$ . More recently, there have been attempts to estimate  $M_{\text{BH}}$  in individual objects independent of a virial coefficient by modeling

reverberation-mapped data directly and constraining the geometry and kinematics of the BLR (see e.g., Pancoast et al. 2014, and references therein).

Seyfert galaxies are low luminosity AGNs for which the host galaxy can be easily resolved, thus making them attractive targets for the study of the  $M_{\text{BH}}$  scaling relations. In fact, for a few Seyfert galaxies,  $M_{\text{BH}}$  estimates from both dynamical AO measurements as well as reverberation mapping are available (Hicks & Malkan 2008). Seyfert galaxies are categorized into different types based on their emission line profiles, ranging from type-1 to type-2 with subclasses (type-1.5, 1.8, and 1.9) in-between. Type-1 Seyferts display both broad and narrow components of emission lines, while type-2 Seyferts show only the narrow components. The intermediate Seyfert types show varying levels of broad component emission. The Balmer series in the optical regime is generally used to classify Seyfert type (Osterbrock & Koski 1976; Osterbrock 1977, 1981, Table 1 summarizes the different Seyfert-type classifications).

In the framework of the so-called standard unified model for active galaxies, all Seyfert galaxies are thought to be intrinsically the same but viewed from a different angle. The key to this model is a region of cold gas and dust, called the dusty torus, that surrounds the BLR and, if seen edge on, can shield both the accretion disk continuum and the broad emission lines from the observer’s view, resulting in a type-2 Seyfert galaxy. If seen face on, however, both accretion disk and BLR are visible, resulting in a type-1 Seyfert galaxy. Intermediate types-1.5, 1.8, and 1.9 are viewed along the edges of the dusty torus where it is not optically thick enough to fully block the broad lines. In other words, in this simplified

model, the presence or absence of broad lines is attributed solely to viewing orientation, meaning that the Seyfert type of a galaxy does not change. (Note that the orientation of the torus is entirely independent of the host-galaxy orientation.)

However, there have been many reports of apparent Seyfert-type changes in the literature (e.g., [Tohline & Osterbrock 1976](#); [Kollatschny & Fricke 1985](#); [Storchi-Bergmann et al. 1993](#); [Aretxaga et al. 1999](#); [Eracleous & Halpern 2001](#); [Trippe et al. 2008](#); [Denney et al. 2014](#); [Shappee et al. 2014](#); [Parker et al. 2015](#)). These changes can occur in either direction. NGC 4151 is one of the most notable and cited examples. Originally classified as a type-1.5 ([Osterbrock 1977](#)), the broad emission lines disappeared throughout the 1980's ([Antonucci & Cohen 1983](#); [Lyutyi, Oknyanskii & Chuvaev 1984](#); [Penton & Perez 1984](#)), but have returned since ([Shapovalova, Popovic & Burenkov et al. 2010](#)). Another well-studied example is Mrk 590 which has been observed over a 40-year time scale. First observed as a type-1.5, Mrk 590 transitioned to a type-1 before the broad lines disappeared, making it a type~1.9-2 Seyfert ([Denney et al. 2014](#)). Possible causes of these changing-look AGNs include changes in extinction (due to our line-of-sight grazing the dusty torus, for instance; e.g., [Goodrich 1989](#); [Leighly et al. 2015](#)), or changes in the AGN accretion rate (e.g., [Nicastro 2000](#); [Korista & Goad 2004](#); [Elitzur, Ho, & Trump 2014](#)) In rare cases, the increase in accretion rate could be due to the tidal disruption and accretion of a star, and a few cases of dramatic broad-line variability possibly linked to this scenario, have been reported in recent years (e.g., [Komossa et al. 2008](#); [Arcavi et al. 2014](#); [LaMassa et al. 2015](#); [Merloni et al. 2015](#)).

A certain degree of variability in the flux and profile of the BLR emission, as a response to changes in the continuum flux (and thus accretion), is not only expected, but in fact forms the basis for reverberation mapping studies. Such studies have shown that variations in continuum flux and that of the broad Balmer lines are correlated in a way so that the derived  $M_{\text{BH}}$  does not change ([Bentz et al. 2007](#); [Park et al. 2012](#); [Barth et al. 2015](#)). However, extreme variability leading to a type change seems to be rare.

Here, we address the question of the frequency of these changing-look AGNs by taking advantage of a statistical sample of 102 local Seyfert galaxies with archival spectra from the Sloan Digital Sky Survey (SDSS) and high-quality Keck spectra taken  $6.4 \pm 1.8$  years apart. The paper is organized in the following manner. Section 2 summarizes the sample selection, observations, and data reduction. Section 3 describes the analysis of the data. Section 4 discusses the derived quantities and results from the data. Section 5 concludes with a summary. The appendix contains a table of observations and Seyfert-type transitions for the sample (A), comparison of SDSS and Keck spectra (B), fits to the SDSS and Keck spectra (C), and SDSS optical images for two extreme objects (D). Throughout the paper, a Hubble constant of  $H_0 = 70 \text{ km s}^{-1}$ ,  $\Omega_\lambda = 0.7$ , and  $\Omega_M = 0.3$  is assumed.

## 2. SAMPLE SELECTION, OBSERVATIONS, AND DATA REDUCTION

The primary goal behind sample selection and observations is the creation of a local baseline for the BH mass scaling relations of active galaxies, presented by [Bennert et al. \(2011\)](#); [Harris et al. \(2012\)](#); [Bennert et al. \(2015\)](#). These papers describe the sample selection, Keck observations, and Keck data reduction in detail. We here provide a brief summary only.

### 2.1. Sample Selection

A sample of 102 local ( $0.02 \leq z \leq 0.1$ ) type-1 Seyfert galaxies was selected from the SDSS data release six (DR6) ([Adelman-McCarthy et al. 2008](#)). Objects were selected on the basis of a broad  $H\beta$  emission line with an estimated  $M_{\text{BH}} > 10^7 M_\odot$  ([Bennert et al. 2011](#); [Harris et al. 2012](#)). Note that of these 102 objects, only 79 are used by [Bennert et al. \(2015\)](#) to study the  $M_{\text{BH}}-\sigma$  relation, since the necessary quantities (i.e.,  $\lambda_{\text{L5100}}$ ,  $M_{\text{BH}}$ ,  $\sigma$ ) for that study were only accessible for these 79 objects.

### 2.2. SDSS Observations and Data Reduction

SDSS spectra are obtained from a 2.5-m ground based telescope with a 3" diameter circular optical fiber and an exposure time of 54 seconds. SDSS spectra cover a wavelength range of  $3800\text{\AA}$  to  $9200\text{\AA}$  with an instrumental resolution of  $170 \text{ km s}^{-1}$ . SDSS data are already fully reduced and flux calibrated when retrieved from the SDSS archive.

### 2.3. Keck Observations and Data Reduction

The 102 objects selected from SDSS were observed again between January 2009 and March 2010 with the Low Resolution Imaging Spectrometer (LRIS) at the Keck 10-m telescope using a 1" x 2" wide rectangular long slit aligned with the major axis of the host galaxy (given by SDSS). (While all objects were observed at as low airmass as possible, given observation constraints, for individual objects the airmass can be as high as 1.4.) Objects observed in 2009 used a D560 dichroic, and objects observed in 2010 used a D680 dichroic. The blue Keck spectra were taken with the 600/400 grism giving a wavelength range of  $\sim 3200\text{-}5350\text{\AA}$  and an instrumental resolution of  $\sim 90 \text{ km s}^{-1}$ ; the red spectra were taken with the 831/8200 grating centered on  $8950\text{\AA}$  with a resolution of  $\sim 45 \text{ km s}^{-1}$ . (Note that the red Keck spectra are not used in this paper since they only cover the Ca triplet absorption lines for an accurate measurement of  $\sigma$ .) The exposure times generally range from 600 to 1200 s. Keck spectra were taken on average  $6.4 \pm 1.8$  years after the SDSS spectra, ranging from 2.6 to 9.1 years (see Table A1 for details on SDSS and Keck observations).

The Keck data are reduced following standard reduction steps such as bias subtraction, flat field correcting, cosmic ray rejection, and wavelength calibration. AOV Hipparcos stars were used to correct for telluric absorption and relative flux calibration. Note that, unlike SDSS spectra, Keck spectra are not absolute flux calibrated because observing conditions were typically not photometric. 1D spectra were extracted from the 2D spectra with a width of  $1.08''$  (8 pixels) to encompass the BLR, given the slit width of  $1''$  and a typical seeing of  $1''$ .

### 2.4. Lick Observations and Data Reduction

For eight objects with significantly weaker or apparently absent broad  $H\beta$  emission in the Keck spectra, follow-up observations were conducted in January and March of 2013 with the 3m Shane telescope of Lick observatory using the Kast spectrograph and 60 min total exposure time per object. (Table A1; [Scott 2013](#)). The slit was aligned either along the major axis or perpendicular to it. 1D spectra were extracted using a 4 pixel ( $\approx 3''$ ) width centered on the peak flux to mimic the 3" diameter circular fiber of SDSS. The data were reduced following standard procedures. The Lick spectra are presented

by Scott (2013). These spectra are used to determine their Seyfert type, since they also cover the H $\alpha$  region. The Seyfert types based on the Lick spectra are listed in Table A1.

### 3. ANALYSIS

In this paper, we focus on four different sets of spectra, for short called “Keck subtracted,” “Keck unsubtracted,” “SDSS subtracted,” and “SDSS unsubtracted,” as explained in the next two sections.

#### 3.1. Unsubtracted Spectra

To classify Seyfert type and perform a qualitative comparison of the H $\beta$  region, the reduced spectra are used. Throughout the paper, these spectra are referred to as the unsubtracted data set.

For a visual comparison of both data sets (Appendix B), the Keck spectra were re-binned to match the lower spectral resolution of the SDSS spectra. For visual presentation purposes of a direct comparison between both spectra in Figures B, the spectra were normalized to constant 5007Å [OIII] emission, assuming that the 5007Å [OIII] emission line flux is identical in both data sets, given that emission from the extended NLR does not vary over the observed timescales. This scaling also assumes that both spectra integrate the same [OIII] emission over the same area which might not necessarily be the case, given the different apertures used. Aligning the long Keck slit along the major axis of the host galaxy may reduce any difference in [OIII] flux covered. However, we discuss aperture effects in more detail below.

#### 3.2. H $\beta$ Fitting and Subtracted Spectra

A multi-component spectral decomposition is used to fit the region around H $\beta$ . The procedure is summarized here briefly (see Park et al. 2015, for details).

First, the observed continuum is modeled and subtracted by fitting a pseudo-continuum consisting of the featureless AGN power-law continuum, host-galaxy starlight templates from the Indo-US spectral library (Valdez et al. 2004), and the AGN FeII emission template from Boroson & Green (1992) for the Keck spectra and from Kovacevic et al. (2010) for the SDSS spectra<sup>1</sup>. Then, the continuum-subtracted H $\beta$  line region is modeled by fitting Gauss-Hermite series (van der Marel & Franx 1993; Woo et al. 2006; McGill et al. 2008) simultaneously to the [OIII] narrow emission lines  $\lambda\lambda 4959, 5007\text{\AA}$  and the broad and narrow H $\beta$  lines, to allow for the fitting of asymmetries. Gauss-Hermite polynomials of order 3-6 are used to fit the broad H $\beta$  line and 7-12 for each [OIII] line. In cases where the HeII  $\lambda 4686\text{\AA}$  emission line is blended with the broad H $\beta$ , the broad and narrow HeII were fitted by simple Gaussian functions.

Depending on the degree of overlap of the broad H $\beta$  component with the [OIII] lines, we model the H $\beta$  line region in two slightly different ways. If there is no blending between the broad H $\beta$  component and the [OIII] $\lambda 5007\text{\AA}$  line, we create a template for the narrow line components by fitting the [OIII] $\lambda 5007\text{\AA}$  line with a Gauss-Hermite series function. The [OIII] $\lambda 4959\text{\AA}$  line is then subtracted by blueshifting the template with a flux scale ratio fixed to 1:3 (see, e.g.,

<sup>1</sup> The two different FeII templates are being used due to the different wavelength ranges covered by the Keck and SDSS spectra. The Keck spectra do not extend far enough into the red to fit the FeII features around 5200Å with the Kovacevic et al. (2010) multi-component template and instead must be fitted with the monolithic template from Boroson & Green (1992).

Dimitrijević et al. 2007, and references therein). Then, the broad and narrow H $\beta$  components are fitted simultaneously through  $\chi^2$ -minimization, using the blueshifted template from the [OIII] $\lambda 5007\text{\AA}$  line as a template for the narrow H $\beta$ , with the flux ratio as a free parameter, and a Gauss-Hermite series for the broad H $\beta$  component.

If the broad H $\beta$  component is heavily blended with the [OIII] doublet lines, we model the H $\beta$  broad and narrow lines and the [OIII] $\lambda\lambda 4959, 5007\text{\AA}$  lines all together by simultaneously fitting a Gauss-Hermite series function to the broad H $\beta$  component and another Gauss-Hermite series function to the [OIII] $\lambda 5007\text{\AA}$  line, where the model for the [OIII] $\lambda 5007\text{\AA}$  line is blueshifted and also used for both the [OIII] $\lambda 4959\text{\AA}$  line with a 1:3 flux scale ratio and the narrow H $\beta$  component with a free flux scale ratio. This approach is based on the known fixed flux ratio of [OIII] $\lambda\lambda 4959, 5007$  of 1:3 and the fact that the [OIII] lines and the narrow H $\beta$  lines originate in the NLR and should have comparable widths. It is an approach typically used to fit AGN spectra in e.g., reverberation mapping studies (Park et al. 2015; Barth et al. 2015).

The results of the spectral fitting are given in Table A2, fits are shown in Appendix C. The pure emission-line spectra – with host-galaxy, power-law continuum and FeII emission subtracted – are referred to in the following as the subtracted data.

Note that for one object in the sample (1655+2014), the S/N ratio is too low (in both SDSS and Keck spectra) for an accurate measurement of the broad H $\beta$  line. For three other objects (0932+0405, 0847+1824, and 0831+0521), the broad H $\beta$  component could not be accurately identified in the Keck spectra. These four objects are excluded from any discussion involving the H $\beta$  line fitting.

#### 3.3. Seyfert-Type Classification

The Seyfert type for all objects was classified independently by eye by two members of the team (JNR & MC) following Table 1, and has been verified independently by the broad H $\beta$  emission-line fitting results. Table A1 lists the Seyfert-type classifications for both SDSS and Keck spectra, as well as the eight objects observed at Lick. Typically, the H $\alpha$  and H $\beta$  lines are used for Seyfert-type classification, and we followed that procedure for the SDSS and Lick spectra. However, the Keck spectra do not extend to the H $\alpha$  line. Instead, higher order Balmer lines (H $\gamma$  and H $\delta$ ) were used as a proxy, see Table 1 (Osterbrock 1977). However, these lines are intrinsically much fainter than H $\alpha$  and H $\beta$ ; for example, assuming case B recombination, H $\delta$  (H $\gamma$ ) is  $\sim 26\%$  (47%) the strength of H $\beta$  which itself is approximately 35% of H $\alpha$  (Osterbrock 1989). Moreover, the H $\gamma$  line is often blended with the 4383Å FeI and the 4363Å [OIII] lines, cautioning the use of this line for classification. Thus, we rely on the H $\beta$  line for classification. This implies that we cannot differentiate between types-1.9 and 2 for Keck spectra. We conservatively classify an object without a broad H $\beta$  line in the Keck spectra as a type-1.9. Note that given the lower S/N of the SDSS spectra, caution should be exercised when classifying the Seyfert sub-types (1.5, 1.8, and 1.9) since broad lines can be easily lost in the noise. However, given that these are all local Seyfert galaxies, generally, S/N ratios are good even for the SDSS spectra. The observed variability of the broad H $\beta$  line is substantial and the overall trend is for a weaker broad H $\beta$  line in Keck, partially due to selection effects (see discussion below).

For a more quantitative determination of Seyfert type, we

used the  $H\beta$  broad/narrow peak-flux ratios and compared them to the visual classification. The reason for choosing peak-flux ratios are threefold. (i) Using flux ratios eliminates uncertainties on absolute flux calibration. Moreover, compared to integrated flux ratios, (ii) peak-flux ratios are essentially driving the visual classification scheme; and (iii) the width of the broad  $H\beta$  line can have large uncertainties and depends strongly on the placement of the continuum. Depending on the signal-to-noise (S/N) of the data, it can easily be either lost in the noise or noise can be fitted as a broad  $H\beta$  line. Thus, integrated-flux ratios are more uncertain than peak-flux ratios.

While there is scatter between these two different classification approaches, we determined cutoffs in the  $H\beta$  broad/narrow peak flux ratios by minimizing the number of outliers. For a peak-flux ratio  $\geq 1.25$  there is an 83% chance that the object is a type-1, for  $1.25 \geq \text{peak-flux ratio} \geq 0.6$ , there is a 67% chance that the object is a type-1.5, and for a peak-flux ratio  $\leq 0.6$  there is a 72% chance that the object is a type-1.8. All type-1.9 objects have a peak-flux ratio of 0, since there is no broad  $H\beta$  component. Below (Section 4.1), we discuss the results based on both visual classification as well as peak-flux ratios. The peak-flux ratios are given in Table A1.

## 4. RESULTS AND DISCUSSION

### 4.1. Seyfert-Type Transitions

Based on our visual classifications, at least some degree of type transition is exhibited by 39/102 objects ( $39 \pm 10\%$ ). To quantify the ‘‘magnitude’’ of the transition, we assign a value between +4 and  $-4$  in increments of 1, with a positive value if the broad  $H\beta$  line weakened between SDSS and Keck. Type changes of +4 indicate a full type transition from type-1 to 2; +3 indicates the object transitioned three types (e.g., 1 to 1.9); +2 indicates a transition of two types (e.g., 1 to 1.8); and +1 indicates a transition of one type (e.g., 1 to 1.5); 0 indicates that the object did not experience a Seyfert-type change. A negative value implies that the  $H\beta$  line increased between SDSS and Keck. Figure 1 shows the distribution of the type transitions quantified in this way.

While there are type transitions in either direction, there are more objects that transition towards a narrower/weaker broad  $H\beta$  line in Keck (transition towards type-2) which is likely a reflection of our sample selection, since only Seyfert galaxies with a broad  $H\beta$  component were selected from SDSS (Bennert et al. 2011; Harris et al. 2012). Of the 39 objects with a type transition, the majority (31) experiences only a minor type change ( $\pm 1$  magnitude transition), while eight underwent greater type changes of 2. One object (0847+1824) demonstrated a type transition of magnitude 3. We consider three objects (3% of the sample) extreme objects since they all show cases of a disappearing broad  $H\beta$  line between SDSS and Keck. We discuss them in detail in Section 4.3. There is no correlation between the magnitude of the type transition and the time between observations, indicating that a Seyfert-type change happens on shorter time scales than those covered by our observations ( $6.4 \pm 1.8$  years).

If we instead use our peak-flux ratio cutoffs, as discussed in Section 4.1, to classify the Seyfert type, the results change only slightly. 46/102 objects undergo a type transition, with the majority (39) experiencing only a minor type change ( $\pm 1$  magnitude transition), while 7 underwent greater type changes of 2. However, we consider the visual classification

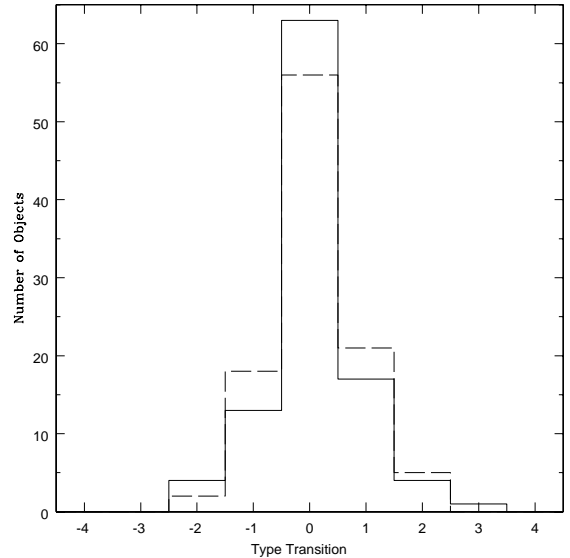


**Figure 1.** Magnitude of Seyfert-type transitions from visual classification (solid line) and peak-flux ratio (dashed line; see text for details).

more reliable, and it is also commonly used in the literature. Thus, in the following we refer to the visual classification.

As outlined in the introduction, AGN type changes have previously been observed in the literature and are often referred to as ‘‘changing-look’’ AGNs (see, e.g., Denney et al. 2014; LaMassa et al. 2015; Runnoe et al. 2016, and references therein); indeed, the frequency and strength of our observed  $H\beta$  emission line variability is in line with one of the first studies on this topic (Rosenblatt et al. 1994).

Two common explanations of type transitions are variable accretion and variable obscuration. Variable accretion, caused by fluctuating amounts of gas available to feed the BH (Bochkarev 2006), results in a change of the continuum flux and subsequently in a change of the broad  $H\beta$  emission line flux, since the BLR clouds are photoionized by the UV continuum. There are many papers citing variable accretion as the driving force behind Seyfert-type transitions (Eracleous & Halpern 2001; Trippe et al. 2008; Shappee et al. 2014; Denney et al. 2014). Denney et al. (2014) is the most notable example reporting Mrk 590 to transition from type-1.5 to type-1, then transition again to type  $\sim 1.9$ -2. Shappee et al. (2014) (for NGC 2617), Trippe et al. (2008) (for NGC 2992), and Antonucci & Cohen (1983) (for NGC 4151) report an observed change in X-ray flux that is followed by a similar change in UV/optical flux. Variable extinction can occur when dusty clouds pass our line-of-sight. For Seyfert galaxies, the source of this obscuration is likely the dusty torus, thought to surround the BLR in the framework of the standard unified model. The individual cold gas clouds of the dusty torus are not all identical and uniform, so different gas clouds could shield different amounts of continuum and  $H\beta$  flux.

The disappearance of broad lines as seen in 3% of our sample (discussed in detail in Section 4.3) has also been documented before. In particular, Ho & Kim (2009) report that ten of the 94 objects in their local sample ( $\sim 11\%$ ), selected to investigate relationships between  $M_{\text{BH}}$  and host galaxy properties using Magellan spectra (3600-6000Å wavelength range), had only narrow lines when the same objects were previously

**Table 1**  
Seyfert-Type Classifications

Type (1)	Description (2)
Type-1	Both broad and narrow components in all Balmer lines.
Type-1.5	Broad and narrow components can be identified in H $\alpha$ and H $\beta$ . Broad component of higher order Balmer lines are weakening.
Type-1.8	Broad H $\beta$ is weak but detectable. No higher order Balmer lines have a broad component.
Type-1.9	Shows broad H $\alpha$ but no higher order Balmer lines have a broad component.
Type-2	No broad emission lines.

**Note.** — Col. (1): Seyfert type. Col. (2): Seyfert-type classification based on the strength of the H $\beta$  and H $\alpha$  lines (Osterbrock 1977, 1981).

classified as type-1 Seyferts. (Note that Ho & Kim 2009 do not discuss this matter further, since it was not the main purpose of their paper.)

In a sample of 117 changing-look quasar candidates selected from SDSS DR12, Ruan et al. (2015) discovers two new low-redshift quasars (in addition to the one previously found by LaMassa et al. 2015) where both the broad H $\beta$  and continuum luminosity dim over the 5–7 years in rest-frame time, changing the objects from quasar-like to galaxy-like states. Ruan et al. (2015) argue that the observed change is driven by rapidly decreasing accretion rates.

From a sample of 1011 low-redshift quasars ( $z < 0.63$ ), selected based on repeated photometry from SDSS and Pan-STARRS1 as well as repeated spectra from SDSS and SDSS-III Boss, MacLeod et al. (2015) visually identify ten changing-look quasars, with 4/10 of these objects showing emission lines broadening with at least a one magnitude increase in g-band flux and 5/10 of these objects having disappearing broad emission lines and a decreasing light curve (one of these five objects was discovered by LaMassa et al. 2015). One of these five objects (SDSS J1021+4645) experienced a type transition from type-1 to type-1.9. MacLeod et al. (2015) report significant changes on timescales of  $\sim 2000$ –3000 days with broad emission line changes corresponding to continuum changes. Variable accretion and obscuration were both discussed as possible options to explain the observed broad-line changes, and neither possibility was ruled out (MacLeod et al. 2015). A tidal disruption flare event might explain the observed changes behind J0159+0033 (MacLeod et al. 2015; Merloni et al. 2015).

For the purpose of a reverberation mapping campaign, Barth et al. (2015) re-observed AGNs classified as Seyfert-1 galaxies based on SDSS spectra 5–8 years later with the 3m Shane telescope of Lick observatory and noted that for one object (NGC 6423), all emission lines had disappeared, and three other objects (Mrk 474, Mrk 728, and Mrk 1494) changed from Seyfert-1 to Seyfert 1.9. We will discuss possible explanations for such extreme changes in Section 4.3.

#### 4.2. Quantifying the Observed Broad H $\beta$ -Line Changes

We use several measurements from our spectral decomposition of the H $\beta$  region discussed in Section 3.2 to further quantify the observed broad H $\beta$  line changes and explore possible origins, particularly in these four quantities: (i) the second moment of the broad H $\beta$  component ( $\sigma_{H\beta}$ ) from the model, used to calculate  $M_{BH}$  (Bennert et al. 2011, 2015) (ii) the full width at half maximum (FWHM) of the broad H $\beta$  line also sometimes used to calculate  $M_{BH}$  (e.g., Shen et al. 2008, 2011)<sup>2</sup> (iii) the flux ratio of the narrow H $\beta$

component and [OIII] lines, H $\beta_{narrow}/[OIII]$  (iv) the peak-flux ratio of the broad and narrow components of the H $\beta$  line, H $\beta_{broad}/H\beta_{narrow}$ . In Figure 2, we compare these four quantities as derived from the SDSS spectra with those derived from the Keck spectra.

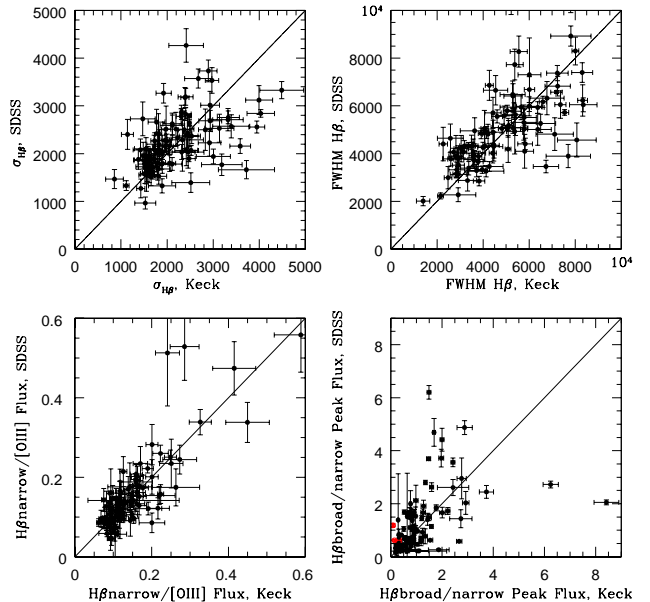


**Figure 2.** Derived quantities from H $\beta$  line fitting of SDSS spectra (y-axis) vs. Keck spectra (x-axis; including a unity line). Top left:  $\sigma_{H\beta}$ . Top right:  $FWHM_{H\beta}$ . Bottom left: H $\beta_{narrow}/[OIII]$  flux ratio. Bottom right: H $\beta_{broad}/H\beta_{narrow}$  peak flux ratio. The two objects shown in red in this panel were classified as 1.9 in the Keck spectrum, thus they do not have a broad component in H $\beta$  and this comparison uses an upper limit on the flux if a broad component were included.

On average, the broad H $\beta$  line is wider in the SDSS spectra than in the Keck spectra, both in  $\sigma_{H\beta}$  ( $1.07 \pm 0.29$ ) and  $FWHM_{H\beta}$  ( $1.08 \pm 0.27$ ) (Table 2). Moreover, the broad H $\beta$  line has more peak flux in the SDSS spectra than in the Keck spectra ( $1.26 \pm 0.12$ ). The broader and stronger H $\beta$  line preferentially in the SDSS spectra is likely attributed to the bias in the sample selection, since only objects with a broad H $\beta$  line were chosen from SDSS.

What is noticeable in the top left panel of Figure 2 is the large scatter: for individual objects,  $\sigma_{H\beta}$  can be almost up to a factor of two different between the two sets of spectra. FWHM follows a similar trend. Reverberation mapping studies have shown that the variability of the line-width in AGNs correlates inversely with the variability of the power-law continuum in a way that it cancels out in the virial product, re-

<sup>2</sup> For a Gaussian profile,  $FWHM_{H\beta} = 2.35\sigma_{H\beta}$ .

sulting in a constant  $M_{\text{BH}}$  measurement, to within  $\sim 0.05$  dex uncertainty (see, e.g., [Bentz et al. 2007](#); [Park et al. 2012](#); [Barth et al. 2015](#)). [Ruan et al. \(2015\)](#) also find that for their changing-look quasars, the decrease in luminosity coincides with a broadening of the line widths to preserve the derived  $M_{\text{BH}}$ . Unfortunately, we cannot test this correlation in this paper, because we derive the host-galaxy free continuum flux from a 2D image decomposition of the SDSS images ([Bennert et al. 2015](#)), taken at yet a different time from the two sets of spectra. We consider this approach superior over spectral decomposition, given unknown aperture effects for spectra. (For the same reason, image decomposition based on typically an HST image taken at a different time is also used for reverberation mapped AGNs (e.g., [Bentz et al. 2013](#).) Moreover, the Keck spectra are not absolutely flux calibrated due to typically non-photometric observing conditions. However, using the same continuum flux, derived from the 2D image decomposition, but taking into account the different width of  $H\beta$  between the SDSS and Keck spectra, the resulting  $M_{\text{BH}}$  is on average  $0.05 \pm 0.03$  dex larger for SDSS spectra. This is small compared to the uncertainty of single-epoch measurements of 0.4 dex. (Note that this includes only the 79 objects from [Bennert et al. \(2015\)](#), since we do not have continuum measurement for the other objects. Also, for obvious reasons, it excludes any object without broad  $H\beta$  emission in the Keck spectra.)

The lower left panel of Figure 2 shows that while overall, the  $H\beta_{\text{broad}}/[\text{OIII}]$  flux ratio as measured in the SDSS spectra is comparable to that in the Keck spectra (on average  $1.04 \pm 0.32$ ) with the majority of the objects falling near the unity line, the scatter is large due to some extreme outliers. While the large scatter could partially be due to the change in broad  $H\beta$  (as a consequence of the observed Seyfert-type change) effecting the narrow  $H\beta$  flux for fitting reasons since the lines are blended, we consider such an effect negligible given the quality of our data and our fitting procedure. More likely, it might indicate that the NLR emission lines are not constant over the timescales of these observations but do indeed reverberate, in line with recent studies by [Peterson et al. \(2013\)](#); [Barth et al. \(2015\)](#).

In the lower right panel of Figure 2, the broad  $H\beta$  to narrow  $H\beta$  peak-flux ratio varies quite a bit between SDSS and Keck spectra ( $1.26 \pm 0.12$ ). This reflects the change in the broad  $H\beta$  emission line, and, as a consequence, Seyfert type. On average, the broad  $H\beta$  line is stronger in the SDSS spectra than in the Keck spectra, most likely due the selection bias. The change in peak-flux ratio can be used as an independent way to classify Seyfert-type transitions, as discussed in Section 4.1.

Reverberation mapping studies have revealed an anti-correlation between broad  $H\beta$  width and luminosity ([Denney et al. 2009](#); [Park et al. 2012](#); [Barth et al. 2015](#)), which is attributed to the relation between ionizing flux and the local re-processing efficiency of the BLR gas: the  $H\beta$  re-processing efficiency is greatest in the outer part of the BLR where the flux from the continuum is lower ([Korista & Goad 2004](#); [Goad & Korista 2014](#)). Therefore, higher levels of continuum luminosity lead to an increase in emissivity-weighted BLR radius. This so-called breathing effect increases flux for low-velocity line core relative to high-velocity wings, which makes the line profile narrower. BLR breathing occurs on short timescales of days to weeks in response to AGN continuum variations. However, our data do not generally support this special kind of line variability.

Variable accretion and/or variable obscuration are considered the two main causes for a type change. As discussed above, to distinguish between them, the variability in X-ray, UV, and optical is typically studied. However, we do not have X-ray data concurring with the SDSS and Keck spectra. Fig. B1–B4 show a qualitative comparison between the change in  $H\beta$  and power-law, overlaying the unsubtracted spectra of SDSS and Keck for each object, scaled to  $[\text{OIII}]$ . There are 41/102 ( $\sim 40\%$ ) objects that have a stronger power-law emission in Keck than SDSS, for 17/102 ( $\sim 17\%$ ) it is the other way around, and 44/102 ( $\sim 43\%$ ) show no notable change. The higher fraction of non-stellar (power-law) continuum in the Keck spectra is explainable by the smaller slit and sharper seeing.

In other words, both the broad  $H\beta$  emission line, as well as the power-law continuum, are varying between the two set of spectra. However, when attempting to quantify those changes, we do not find them to be directly correlated. This is not too surprising, since any variation between broad  $H\beta$  emission and power-law continuum are offset in time depending on the time-lag of a given object and would not show up at the same time in a single-epoch spectrum (see e.g., Figs. 7 & 8 in [Park et al. 2012](#)).

Aperture effects may play a role in our results: Keck spectra ( $1'' \times 1''$  square), given the seeing, only include the unresolved emission from BLR, AGN power-law continuum, and NLR, while the SDSS spectra ( $1.5''$  radius circular fiber) may additionally include more extended NLR flux. However, any aperture effect would artificially boost the ratio of broad-to-narrow flux in Keck spectra (both peak and integrated) compared to SDSS spectra, since Keck spectra are restricted to a smaller central area and thus focus on the unresolved emission. Thus, aperture effects cannot explain the opposite trend that we are observing in the majority of objects, namely, that we observe less broad  $H\beta$  in the Keck spectra.

We note that a few objects (e.g., 0909+1330, 1312+2628, 1708+2153, 2140+0025) show significantly stronger blue continuum emission (Fig. B1–B4). This rise in the blue wavelength range cannot simply be explained by the fact that the Keck spectra were not obtained at parallactic angle since this would have the opposite effect. Similarly, none of the SDSS spectra were taken at large airmasses, with the exception of 2140+0025 that was observed at an airmass of 1.3, which could have reduced the blue wavelengths emission artificially for that object in the SDSS spectrum. To further test whether the rise in the blue wavelengths emission in the Keck spectra compared to SDSS is an artifact of Keck flux calibration, we looked at the spatially-resolved spectra. The rise in the blue continuum is only present in the central spectra within the seeing limits, but not in the outer spectra, suggesting that it is a real trend. A stronger power-law continuum may indeed explain the Seyfert-type change observed for 0909+1330 (from 1.8 in SDSS to 1 in Keck) and 1708+2153 (from 1.5 in SDSS to 1 in Keck). (Note that the other two objects were classified as Seyfert-1 in both spectra). However, as mentioned above, part of this higher fraction of power-law continuum in the Keck spectra can simply be due to the smaller aperture and sharper seeing compared to SDSS.

#### 4.3. Extreme Seyfert-Type Changes

For three objects in the sample, the broad  $H\beta$  component was very prominent in the SDSS spectra, but decreased significantly and virtually disappeared in the Keck spectra. All three were re-observed with the 3m Shane telescope of Lick

**Table 2**  
Comparison between SDSS and Keck

Data (1)	Average (2)
$\sigma_{H\beta}$	$1.07 \pm 0.03$
$\text{FWHM}_{H\beta}$	$1.08 \pm 0.03$
$H\beta_{\text{narrow}}/[\text{OIII}]$	$1.04 \pm 0.03$
$H\beta_{\text{broad}}/H\beta_{\text{narrow}}$	$1.26 \pm 0.12$

**Note.** — Col. (1): Comparison between values derived from the SDSS spectra vs. those derived from the Keck spectra for quantities listed in this column. Col. (2): Average and scatter.

observatory (Scott 2013). Table 3 summarizes the Seyfert-type changes of these objects. Note that all Keck objects classified conservatively as type-1.9 could be a type-2 object; however, the spectra do not extend to H $\alpha$ , so we cannot distinguish between the two. Especially in those cases where the Lick spectrum reveals a type-2 object, it is likely that the object was also a type-2 in the Keck spectrum. Also note that for 1423+2720, the SDSS spectrum has a low S/N which makes it difficult to model the underlying broad H $\beta$  line.

The continuum luminosity at 5100Å was compared for all objects in the sample in order to determine if there was a correlation between AGN luminosity and strongly variable objects, but no correlation was found.

For all objects, we carefully searched the literature for other optical spectra. 0847+1824 is the only object for which this search was successful: It was previously observed on 02-28-2004 (MJD 53063), before the SDSS observation, and from that spectrum, the AGN was a type-1 Seyfert (Ho & Kim 2009).

Apart from variable accretion and/or obscuration, we briefly discuss a few other scenarios which could mimic changes in Seyfert type.

(i) Telescope offset: First of all, we note that apparent Seyfert-type changes could be caused by a slight mis-pointing of the Keck telescope, missing the AGN core and therefore the (bulk of the) broad emission lines. In all cases, the telescope was pointed at the center of the galaxy (as verified by guide star images), assuming that the AGN resides there. For a couple of extreme objects, the AGN might actually be offset from the center, as evidenced by the SDSS images; we will discuss them below. Note that for all objects for which the AGN core and BLR coincide with the center of the galaxy, the possibility of missing the BLR emission due to a telescope offset is negligible, given the seeing ( $\sim 1''$  for the Keck observations) and the slit width used ( $1''$ , matching the typical seeing), as verified by standard-star observations. Keck telescope guiding is also much more accurate than  $1''$ .

(ii) Galaxy mergers and/or recoiling SMBH: In the course of ongoing galaxy mergers, the AGN can appear offset from the apparent center of the merging system. It is therefore possible that an off-center AGN was captured by the wider, circular SDSS aperture, but missed during subsequent observation by the narrower Keck slit, aligned along the major axis of the galaxy and centered on the galactic nucleus. Alternatively, a rare gravitational wave recoil following the final coalescence of two SMBHs in a merger, can remove the newly formed single SMBH from the center of its host galaxy (e.g., see the review by Sperhake 2015). The accretion disk and BLR would

remain bound, and a recoiling SMBH would therefore appear as an AGN offset from the core of its host galaxy (Komossa 2012), again leading to the possibility of missing the (bulk of the) BLR in the more narrow (and rectangular) Keck slit.

With the exception of a few cases (4/102, see Bennert et al. 2015); there are no signs for merger activity in the sample. However, we caution that merger signatures such as faint tidal tails might easily be missed in the low S/N SDSS images. Objects 0847+1824 and 1038+4658 show extended emission in the SDSS multi-color images, offset from the galaxy center (Fig. D), which might indicate the presence of an ongoing merger. While we cannot exclude the possibility that these are off-center AGNs, it is statistically unlikely to have off-centered AGNs in such a small sample, and follow-up spectroscopy would be needed to test such a scenario further. We note in passing that 0847+1824 seems to show a small kinematic offset between its narrow and broad H $\beta$  line (with the broad H $\beta$  line being blue-shifted by  $\sim 100\text{km s}^{-1}$ ), which is, however, most likely mimicked by the asymmetric broad line profile.

(iii) Supernovae: A type II supernova has many of the same spectral features as a Seyfert galaxy (Filippenko 1997). A nuclear supernova could have therefore mimicked the presence of an AGN. However, supernova spectra including the narrow emission lines evolve rapidly, and we do not see any other signs of dramatic changes in the continuum and narrow emission lines.

(iv) Stellar tidal disruption event: Stars can be tidally disrupted and accreted by SMBHs, producing a luminous accretion flare (e.g., Rees 1988). If these occur in a gas rich environment, broad and narrow emission lines can be temporarily excited. While a few candidate events for this process have been identified recently from SDSS (e.g., Komossa et al. 2008), these events are rare, and are unlikely to occur in our small sample. In particular, we have checked the long-term Catalina lightcurves of all three sources, and none shows the characteristic lightcurve decline expected for a typical tidal disruption event.

We are left with mild changes in accretion or extinction as most likely explanation for the three changing-look AGN in our sample. Future spectroscopic monitoring of emission-line and continuum changes will enable us to distinguish between both possibilities. (Note that a difference in aperture between Keck and SDSS cannot explain the extreme Seyfert-type changes we observe in these three objects since it would have the opposite effect.)

#### 4.4. Comparison with the Catalina Sky Survey

**Table 3**  
Extreme Seyfert-Type Changes

Object	Class. SDSS	Class. Keck	Class. Lick	Notes
(1)	(2)	(3)	(4)	(5)
0847+1824	1	1.9	2	Off-centered emission in SDSS image
1038+4658	1.5	1.9	1.9	Type-1 also in literature spectrum taken $\sim 1.8$ years before SDSS Off-centered blob in SDSS image
1423+2720	1.5	1.9	1.8	Low S/N in SDSS spectrum

**Note.** — Col. (1): Object (for more details see Table A1). Col. (2): Seyfert-type classification based on SDSS spectrum. Col. (3): Seyfert-type classification based on Keck spectrum. Col. (4): Seyfert-type classification based on Lick spectrum. Col. (5): Notes (see text for further discussion).

To further shed light on the causes for the observed variability, we considered the optical light curves in the Catalina Sky Survey (CSS) (Drake et al. 2009). With the exception of 1104+4334 and 1206+4244, all objects in our sample are in the CSS archive. (Note that 1605+3305 is in the archive, but it does not have a light curve available.) For most objects, CSS light curves begin after the SDSS observations, but extend past the time of the Keck and Lick observations; the light curves start and end at approximately  $\sim 53500$ – $56500$  MJD ( $\sim 3000$  days). The light curves of seven objects (0310-0049, 0904+5536, 1147+0902, 1355+3834, 1434+4839, 1535+5754, 1557+0830)<sup>3</sup> reveal large variability ( $\sim 0.5$ -1mag in one object) over time-scales from days to months to years. None of these objects are amongst our extreme subset of objects (see Table A1 for Seyfert types).

Since CSS photometry is aperture based (Drake et al. 2009), we cannot exclude that a variable seeing can mimic variability since more or less of the host galaxy would be included in an aperture centered on the AGN. However, especially the extreme variability in these seven objects is unlikely to be purely a seeing effect. Independent analysis, which is beyond the scope of this paper, is needed to further confirm the observed variability.

## 5. SUMMARY

In this paper, we study the broad  $H\beta$  emission-line variability in a sample of 102 local Seyfert-1 galaxies, selected from SDSS and re-observed 3-9 (on average  $6.4 \pm 1.8$ ) years later with LRIS on the 10m Keck-I telescope.

In the 3–9 year time-frame between observations, 67/102 ( $\sim 66\%$ ) objects show at least some form of variability of either width and/or strength of the broad  $H\beta$  line. For 39/102 ( $\sim 38\%$ ) objects, this variability is significant enough to result in a change in Seyfert type, following the standard Seyfert classification scheme. There is no correlation between the time between observations and the degree of the observed Seyfert-type transition, implying that the transitions happen on shorter time scales. Short-time variability on the scale of days and weeks is known for low-mass AGNs from reverberation mapping. Almost all objects (99/102) were observed as part of the CSS with 7/102 ( $\sim 7\%$ ) displaying significant variability on time scales of days to weeks.

Three ( $\sim 3\%$ ) objects are extreme cases for which the broad  $H\beta$  component almost completely disappears. We discuss

<sup>3</sup> Note that 0301+0110 shows a highly variable light-curve, but upon further inspection, it becomes clear that that is an artifact of a bright nearby star.

possible origins for these transitions. For two of these objects (0847+1824 and 1038+4658), SDSS images reveal extended emission off-centered from the galaxy center that could have been included in the SDSS spectra, but missed by the smaller-area Keck slit centered on the galaxy.

The study presented here is the first to provide statistical information on the frequency and strength of  $H\beta$  line variability in a sample of low-redshift Seyfert galaxies.

We thank the anonymous referee for valuable comments helping to improve the paper. We thank Aaron Barth and Bernd Husemann for helpful discussions, Luis Ho for providing additional data, and William C. Keel for data reduction of the Lick spectra. JNR, MC, and VNB gratefully acknowledge assistance from a National Science Foundation (NSF) Research at Undergraduate Institutions (RUI) grant AST-1312296. Note that findings and conclusions do not necessarily represent views of the NSF. VNB, BS, and SK would like to thank the Kavli Institute for Theoretical Physics (Santa Barbara) for their hospitality and support; the KITP is supported by NSF Grant No. NSF PHY11-25915. D.P. acknowledges support through the EACOA Fellowship from The East Asian Core Observatories Association, which consists of the National Astronomical Observatories, Chinese Academy of Science (NAOC), the National Astronomical Observatory of Japan (NAOJ), Korean Astronomy and Space Science Institute (KASI), and Academia Sinica Institute of Astronomy and Astrophysics (ASIAA). This research has made use of the Dirac computer cluster at Cal Poly, maintained by Dr. Brian Granger and Dr. Ashley Ringer McDonald. Data presented in this thesis were obtained at the W. M. Keck Observatory, which is operated as a scientific partnership among Caltech, the University of California, and NASA. The Observatory was made possible by the generous financial support of the W. M. Keck Foundation. The authors recognize and acknowledge the very significant cultural role and reverence that the summit of Mauna Kea has always had within the indigenous Hawaiian community. We are most fortunate to have the opportunity to conduct observations from this mountain. This research has made use of the public archive of the Sloan Digital Sky Survey (SDSS) and the NASA/IPAC Extragalactic Database (NED) which is operated by the Jet Propulsion Laboratory, California Institute of Technology, under contract with the National Aeronautics and Space Administration. The CSS survey is funded by the National Aeronautics and Space Administration under Grant No. NNG05GF22G issued through the Science Mission Directorate Near-Earth Objects Observations Program. The CRTS survey is supported by the



U.S. National Science Foundation under grants AST-0909182  
and AST-1313422.

Facilities: Keck: I (LRIS), Lick: Shane 3-m Kast spectro-  
graph

## APPENDIX

## A. TABLE OF OBSERVATIONS AND SEYFERT-TYPE CLASSIFICATION

**Table A1**  
Observations and Seyfert-Type Classification

Object	R.A. (J2000)	Dec. (J2000)	$z$	Date SDSS	Class. SDSS	Date Keck	Class. Keck	Exp. time Keck [s]	Diff. years	Date Lick	Class. Lick
(1)	(2)	(3)	(4)	(5)	(6)	(7)	(8)	(9)	(10)	(11)	(12)
0013-0951	00 13 35.38	-09 51 20.9	0.062	08-17-2001 (52138)	1	09-20-2009 (55094)	1.5	600	8.09		
0026+0009	00 26 21.29	+00 09 14.9	0.060	08-26-2000 (51782)	1	09-20-2009 (55094)	1	1600	9.07		
0038+0034	00 38 47.96	+00 34 57.5	0.081	09-06-2000 (51793)	1	09-20-2009 (55094)	1.5	600	9.04		
0109+0059	01 09 39.01	+00 59 50.4	0.093	09-07-2000 (51794)	1.5	09-20-2009 (55094)	1.5	600	9.04		
0121-0102	01 21 59.81	-01 02 24.4	0.054	09-02-2000 (51789)	1.5	01-21-2009 (54852)	1	1200	8.39		
0150+0057	01 50 16.43	+00 57 01.9	0.085	09-06-2000 (51793)	1	09-20-2009 (55094)	1	600	9.04		
0206-0017	02 06 15.98	-00 17 29.1	0.043	09-25-2000 (51812)	1	01-22-2009 (54853)	1	1200	8.33		
0212+1406	02 12 57.59	+14 06 10.0	0.062	12-05-2000 (51883)	1	09-20-2009 (55094)	1	600	8.79		
0301+0110	03 01 24.26	+01 10 22.5	0.072	09-30-2000 (51817)	1.5	09-20-2009 (55094)	1.5	600	8.97		
0301+0115	03 01 44.19	+01 15 30.8	0.075	09-30-2000 (51817)	1	09-20-2009 (55094)	1	600	8.97		
0310-0049	03 10 27.82	-00 49 50.7	0.080	12-15-2001 (52258)	1	09-20-2009 (55094)	1	600	7.76		
0336-0706	03 36 02.09	-07 06 17.1	0.097	12-31-2000 (51909)	1.8	09-20-2009 (55094)	1.8	2400	8.72		
0353-0623	03 53 01.02	-06 23 26.3	0.076	12-30-2000 (51908)	1.8	01-22-2009 (54853)	1	1200	8.06		
0731+4522	07 31 26.68	+45 22 17.4	0.092	11-05-2004 (53314)	1.5	09-20-2009 (55094)	1.5	600	4.87		
0735+3752	07 35 21.19	+37 52 01.9	0.096	11-29-2000 (51877)	1.5	09-20-2009 (55094)	1.8	600	8.81		
0737+4244	07 37 03.28	+42 44 14.6	0.088	01-31-2004 (53035)	1.5	09-20-2009 (55094)	1.5	600	5.64		
0802+3104	08 02 43.40	+31 04 03.3	0.041	01-02-2003 (52641)	1	01-21-2009 (54852)	1	1200	5.97		
0811+1739	08 11 10.28	+17 39 43.9	0.065	12-18-2004 (53357)	1.5	03-15-2010 (55270)	1	2700	5.24		
0813+4608	08 13 19.34	+46 08 49.5	0.054	11-29-2000 (51877)	1.8	01-14-2010 (55210)	1	1200	9.13		
0831+0521	08 31 07.62	+05 21 05.9	0.035	01-07-2003 (52646)	1.8	03-15-2010 (55270)	1.9	600	7.18		
0845+3409	08 45 56.67	+34 09 36.3	0.066	02-02-2003 (52672)	1.5	03-14-2010 (55269)	1.5	3600	7.11		
0846+2522	08 46 54.09	+25 22 12.3	0.051	12-19-2004 (53358)	1.5	01-22-2009 (54853)	1.5	1200	4.09		
0847+1824	08 47 48.28	+18 24 39.9	0.085	12-07-2005 (53711)	1	01-21-2009 (54852)	1.9	1200	3.10	01-15-2013 (56307)	2
0854+1741	08 54 39.25	+17 41 22.5	0.065	12-25-2005 (53729)	1.5	03-15-2010 (55270)	1	600	4.22		
0857+0528	08 57 37.77	+05 28 21.3	0.059	01-31-2003 (52670)	1	01-15-2010 (55211)	1	600	6.96		
0904+5536	09 04 36.95	+55 36 02.5	0.037	12-30-2000 (51908)	1.5	03-14-2010 (55269)	1.5	600	9.20		
0909+1330	09 09 02.35	+13 30 19.4	0.051	04-01-2006 (53826)	1.8	01-14-2010 (55210)	1	600	3.79		
0921+1017	09 21 15.55	+10 17 40.9	0.039	02-15-2004 (53050)	1.8	01-14-2010 (55210)	1.8	700	5.91		
0923+2254	09 23 43.00	+22 54 32.7	0.033	12-23-2005 (53727)	1	01-15-2010 (55211)	1	600	4.06		
0923+2946	09 23 19.73	+29 46 09.1	0.063	01-19-2005 (53389)	1.8	01-15-2010 (55211)	1.8	600	4.99		
0927+2301	09 27 18.51	+23 01 12.3	0.026	12-26-2005 (53730)	1.5	01-15-2010 (55211)	1.5	600	4.05		
0932+0233	09 32 40.55	+02 33 32.6	0.057	02-25-2001 (51965)	1.8	01-14-2010 (55210)	1.5	600	8.88		
0932+0405	09 32 59.60	+04 05 06.0	0.059	12-21-2001	1.8	01-14-2010	1.9	600	8.07	03-11-2013	1.9

Table A1 — *Continued*

Object	R.A. (J2000)	Dec. (J2000)	$z$	Date SDSS	Class. SDSS	Date Keck	Class. Keck	Exp. time Keck [s]	Diff. years	Date Lick	Class. Lick
(1)	(2)	(3)	(4)	(5)	(6)	(7)	(8)	(9)	(10)	(11)	(12)
0936+1014	09 36 41.08	+10 14 15.7	0.060	(52264) 12-20-2003	1.5	(55210) 03-15-2010	1	3600	6.23	(56362)	
0938+0743	09 38 12.27	+07 43 40.0	0.022	(52993) 04-04-2003	1	(55270) 01-14-2010	1.8	600	6.78	01-15-2013 (56307)	1.8
0948+4030	09 48 38.43	+40 30 43.5	0.047	(52733) 03-11-2003	1	(55210) 01-15-2010	1.8	900	6.85		
1002+2648	10 02 18.79	+26 48 05.7	0.052	(52709) 01-22-2006	1.8	(55211) 01-15-2010	1.9	600	3.98		
1029+1408	10 29 25.73	+14 08 23.2	0.061	(53757) 03-11-2004	1.5	(55211) 01-15-2010	1.5	600	5.85		
1029+2728	10 29 01.63	+27 28 51.2	0.038	(53075) 02-28-2006	1.8	(55211) 01-15-2010	1.8	600	3.88		
1029+4019	10 29 46.80	+40 19 13.8	0.067	(53794) 01-29-2004	1.5	(55211) 01-14-2010	1.5	600	5.96		
1038+4658	10 38 33.42	+46 58 06.6	0.063	(53033) 12-12-2002	1.5	(55210) 01-14-2010	1.9	600	7.09	01-17-2013 (56309)	1.9
1042+0414	10 42 52.94	+04 14 41.1	0.052	(52620) 03-06-2002	1.5	(55210) 04-16-2009	1.5	1200	7.11		
1043+1105	10 43 26.47	+11 05 24.3	0.048	(52339) 04-20-2004	1.8	(54937) 04-16-2009	1.8	600	4.99		
1049+2451	10 49 25.39	+24 51 23.7	0.055	(53115) 02-26-2006	1	(54937) 04-16-2009	1	600	3.13		
1058+5259	10 58 28.76	+52 59 29.0	0.068	(53792) 01-13-2003	1.5	(54937) 01-14-2010	1.5	600	7.00		
1101+1102	11 01 01.78	+11 02 48.8	0.036	(52652) 04-24-2004	1.5	(55210) 04-16-2009	1.8	600	4.98		
1104+4334	11 04 56.03	+43 34 09.1	0.049	(53119) 02-18-2004	1.8	(54937) 01-14-2010	1.5	600	5.91		
1110+1136	11 10 45.97	+11 36 41.7	0.042	(53053) 03-14-2004	1.5	(55210) 03-15-2010	1	3600	6.00		
1116+4123	11 16 07.65	+41 23 53.2	0.021	(53078) 12-30-2003	1.8	(55270) 04-15-2009	1.8	850	5.29		
1118+2827	11 18 53.02	+28 27 57.6	0.060	(53003) 02-27-2006	1.8	(54936) 01-15-2010	1.9	900	3.88	03-11-2013 (56362)	1.8
1132+1017	11 32 49.28	+10 17 47.4	0.044	(53793) 05-22-2003	1.5	(55211) 01-15-2010	1	600	6.65		
1137+4826	11 37 04.17	+48 26 59.2	0.054	(52781) 01-03-2003	1.5	(55211) 01-14-2010	1.5	600	7.03		
1139+5911	11 39 08.95	+59 11 54.6	0.061	(52642) 05-15-2002	1	(55210) 01-14-2010	1	600	7.67		
1140+2307	11 40 54.09	+23 07 44.4	0.035	(52409) 05-21-2006	1.8	(55210) 01-15-2010	1.8	1200	3.66	01-13-2013 (56305)	2
1143+5941	11 43 44.30	+59 41 12.4	0.063	(53876) 05-17-2002	1.5	(55211) 03-14-2010	1	3000	7.82		
1144+3653	11 44 29.88	+36 53 08.5	0.038	(52411) 03-13-2005	1	(55269) 04-16-2009	1	600	4.09		
1145+5547	11 45 45.18	+55 47 59.6	0.053	(53442) 04-30-2003	1	(54937) 03-14-2010	1	3600	6.87		
1147+0902	11 47 55.08	+09 02 28.8	0.069	(52759) 05-01-2003	1.5	(55269) 01-15-2010	1.5	600	6.71		
1205+4959	12 05 56.01	+49 59 56.4	0.063	(52760) 06-17-2002	1.8	(55211) 01-14-2010	1.8	600	7.58		
1206+4244	12 06 26.29	+42 44 26.1	0.052	(52442) 04-25-2004	1	(55210) 03-14-2010	1	1100	5.88		
1210+3820	12 10 44.27	+38 20 10.3	0.023	(53120) 04-13-2005	1.5	(55269) 04-16-2009	1.5	600	4.01		
1216+5049	12 16 07.09	+50 49 30.0	0.031	(53473) 05-19-2002	1.8	(54937) 03-14-2010	1.8	900	6.82		
1223+0240	12 23 24.14	+02 40 44.4	0.024	(52413) 01-09-2002	1	(55269) 03-15-2010	1	600	8.18		
1228+0951	12 28 11.41	+09 51 26.7	0.064	(52283) 04-02-2003	1.8	(55270) 03-15-2010	1.8	600	6.95		
1231+4504	12 31 52.04	+45 04 42.9	0.062	(52731) 02-27-2004	1.5	(55270) 01-15-2010	1.5	1200	5.88		
1241+3722	12 41 29.42	+37 22 01.9	0.063	(53062) 04-02-2006	1.5	(55211) 01-15-2010	1.5	800	3.79		
1246+5134	12 46 38.74	+51 34 55.9	0.067	(53827) 04-15-2002	1.8	(55211) 01-15-2010	1.5	600	7.75		
1250-0249	12 50 42.44	-02 49 31.5	0.047	(52379) 03-29-2001	1.5	(55211) 04-16-2009	1.8	1200	8.05		
1306+4552	13 06 19.83	+45 52 24.2	0.051	(51997) 04-22-2004	1	(54937) 03-14-2010	1.5	3600	5.89		
1307+0952	13 07 21.93	+09 52 09.3	0.049	(53117) 05-29-2006	1.8	(55269) 03-15-2010	1.5	2400	3.79		
				(53884)		(55270)					

Table A1 — *Continued*

Object	R.A. (J2000)	Dec. (J2000)	$z$	Date SDSS	Class. SDSS	Date Keck	Class. Keck	Exp. time Keck [s]	Diff. years	Date Lick	Class. Lick
(1)	(2)	(3)	(4)	(5)	(6)	(7)	(8)	(9)	(10)	(11)	(12)
1312+2628	13 12 59.59	+26 28 24.0	0.060	02-28-2006 (53794)	1	03-14-2010 (55269)	1	2700	4.04		
1313+3653	13 13 48.96	+36 53 57.9	0.067	03-21-2006 (53815)	1.8	03-14-2010 (55269)	1.8	600	3.98		
1323+2701	13 23 10.39	+27 01 40.4	0.056	03-01-2006 (53795)	1.8	04-16-2009 (54937)	1.8	700	3.13		
1353+3951	13 53 45.93	+39 51 01.6	0.063	02-26-2004 (53061)	1.8	03-14-2010 (55269)	1.9	600	6.05	03-12-2013 (56363)	1.8
1355+3834	13 55 53.52	+38 34 28.5	0.050	03-31-2005 (53460)	1.8	04-16-2009 (54937)	1.8	300	4.04		
1405-0259	14 05 14.86	-02 59 01.2	0.054	06-18-2002 (52443)	1	04-16-2009 (54937)	1	1600	6.83		
1416+0317	14 16 30.82	+01 37 07.9	0.054	03-26-2001 (51994)	1.5	03-15-2010 (55270)	1.8	2700	8.97		
1419+0754	14 19 08.30	+07 54 49.6	0.056	06-12-2005 (53533)	1.8	04-16-2009 (54937)	1.8	900	3.84		
1423+2720	14 23 38.43	+27 20 09.7	0.064	05-26-2006 (53881)	1.5	03-14-2010 (55269)	1.9	1200	3.80	03-12-2013 (56363)	1.8
1434+4839	14 34 52.45	+48 39 42.8	0.037	04-04-2003 (52733)	1	04-16-2009 (54937)	1.5	600	6.03		
1505+0342	15 05 56.55	+03 42 26.3	0.036	05-26-2001 (52055)	1.5	03-15-2010 (55270)	1.5	1200	8.80		
1535+5754	15 35 52.40	+57 54 09.3	0.030	03-14-2002 (52347)	1	04-15-2009 (54936)	1	1200	7.09		
1543+3631	15 43 51.49	+36 31 36.7	0.067	08-24-2003 (52875)	1	03-15-2010 (55270)	1.5	1200	6.56		
1545+1709	15 45 07.53	+17 09 51.1	0.048	06-03-2006 (53889)	1.8	04-15-2009 (54936)	1	1200	2.57		
1554+3238	15 54 17.42	+32 38 37.6	0.048	07-05-2003 (52825)	1.5	04-15-2009 (54936)	1.5	1200	5.78		
1557+0830	15 57 33.13	+08 30 42.9	0.047	08-11-2004 (53228)	1.5	04-15-2009 (54936)	1.5	1200	4.68		
1605+3305	16 05 02.46	+33 05 44.8	0.053	05-17-2004 (53142)	1	04-15-2009 (54936)	1	1200	4.91		
1606+3324	16 06 55.94	+33 24 00.3	0.059	05-19-2004 (53144)	1.5	04-15-2009 (54936)	1.5	1200	4.91		
1611+5211	16 11 56.30	+52 11 16.8	0.041	05-22-2001 (52051)	1.5	04-15-2009 (54936)	1.8	1200	7.95		
1636+4202	16 36 31.28	+42 02 42.5	0.061	06-23-2001 (52083)	1	03-14-2010 (55269)	1	1200	8.72		
1647+4442	16 47 21.47	+44 42 09.7	0.025	05-22-2001 (52051)	1.8	03-14-2010 (55269)	1.5	4200	8.81		
1655+2014	16 55 14.21	+20 14 42.0	0.084	06-13-2004 (53169)	1.8	09-20-2009 (55094)	1.8	600	5.27		
1708+2153	17 08 59.15	+21 53 08.1	0.072	06-21-2004 (53177)	1.5	09-20-2009 (55094)	1	600	5.25		
2116+1102	21 16 46.33	+11 02 37.3	0.081	07-13-2002 (52468)	1.8	09-20-2009 (55094)	1.8	700	7.19		
2140+0025	21 40 54.55	+00 25 38.2	0.084	07-10-2002 (52465)	1	09-20-2009 (55094)	1	600	7.20		
2215-0036	22 15 42.29	-00 36 09.6	0.099	09-04-2000 (51791)	1	09-20-2009 (55094)	1	600	9.04		
2221-0906	22 21 10.83	-09 06 22.0	0.091	10-21-2001 (52203)	1	09-20-2009 (55094)	1	600	7.92		
2222-0819	22 22 46.61	-08 19 43.9	0.082	10-24-2001 (52206)	1.5	09-20-2009 (55094)	1.5	700	7.91		
2233+1312	22 33 38.42	+13 12 43.5	0.093	09-04-2002 (52521)	1	09-20-2009 (55094)	1.5	800	7.04		
2254+0046	22 54 52.24	+00 46 31.4	0.091	09-02-2000 (51789)	1	09-20-2009 (55094)	1	600	9.05		
2327+1524	23 27 21.97	+15 24 37.4	0.046	11-25-2001 (52238)	1.5	09-20-2009 (55094)	1.8	600	7.82		
2351+1552	23 51 28.75	+15 52 59.1	0.096	11-13-2001 (52226)	1.8	09-20-2009 (55094)	1.8	600	7.85		

**Note.** — Col. (1): Target ID based on R.A. and Dec. used throughout the text. Col. (2): Right ascension. Col. (3): Declination. Col. (4): Redshift from SDSS-DR7. Col. (5): Date SDSS spectrum was taken (with Modified Julian Date (MJD) in brackets). Col. (6): Seyfert-type classification based on SDSS spectrum. Col. (7): Date Keck spectrum was taken (with MJD in brackets). Col. (8): Seyfert-type classification based on Keck spectrum. Note that because Keck spectra do not extend to H $\alpha$ , we cannot differentiate between type-1.9 and type-2, and conservatively classify these objects in question as type-1.9. Col. (9): Exposure time of Keck observations in seconds. Note that the exposure time for all SDSS spectra is 54 seconds. Col. (10): Time between SDSS and Keck observations in years. Col. (11): Date Lick spectrum was taken (with MJD in brackets). Col. (12): Seyfert-type classification based on Lick spectrum.

**Table A2**  
Results from Spectral Fitting

Object	$\sigma_{H\beta}$ SDSS [km s <sup>-1</sup> ]	$FWHM_{H\beta}$ SDSS [km s <sup>-1</sup> ]	$\frac{H\beta_{narrow}}{[OIII]}$ flux SDSS	$H\beta_{broad}$ flux SDSS	$H\beta_{broad}$ peak flux SDSS	FeII SDSS	$\sigma_{H\beta}$ Keck [km s <sup>-1</sup> ]	$FWHM_{H\beta}$ Keck [km s <sup>-1</sup> ]	$\frac{H\beta_{narrow}}{[OIII]}$ flux Keck	$H\beta_{broad}$ flux Keck
(1)	(2)	(3)	(4)	(5)	(6)	(7)	(8)	(9)	(10)	(11)
0013-0951	1783±135	3462±205	0.13±0.02	65±10	8±1	Y	2111±211	4275±594	0.17±0.02	20±2
0026+0009	964±125	2276±293	0.18±0.05	14±4	2.7±0.7	N	1527±227	2920±765	0.26±0.06	10±2
0038+0034	2759±133	7371±321	0.08±0.01	23.2±1.8	1.54±0.09	N	3328±211	7223±593	0.09±0.01	10±1
0109+0059	1677±230	3392±282	0.15±0.02	4.6±0.8	0.70±0.09	Y	1797±268	3377±355	0.11±0.01	4.1±0.8
0121-0102	2070±194	4069±255	0.15±0.03	6±1	0.9±0.2	Y	1742±106	3145±145	0.10±0.01	11±0.9
0150+0057	1799±172	4816±408	0.09±0.01	25±4	2.0±0.2	N	2057±129	4212±242	0.07±0.01	1±4
0206-0017	2514±483	5054±761	0.12±0.03	18±5	1.68±0.18	Y	1979±99	4060±148	0.10±0.01	34±3
0212+1406	1947±198	3776±299	0.11±0.01	15.0±1.9	1.6±0.1	Y	1586±129	2601±242	0.15±0.01	17.7±1.7
0301+0110	2078±226	3751±370	0.47±0.07	4.9±0.8	0.90±0.08	Y	1423±160	3612±442	0.42±0.06	6.77±1.08
0301+0115	1510±182	3928±181	0.05±0.01	39±6	6.2±0.5	Y	1653±105	3594±200	0.09±0.01	16.2±1.6
0310-0049	1713±111	3152±178	0.09±0.01	44±6	2.9±0.4	Y	1558±69	2843±153	0.08±0.02	70±12
0336-0706	3189±177	6827±416	0.19±0.02	4.8±0.4	0.32±0.02	Y	2403±164	7238±552	0.16±0.04	3.6±1.3
0353-0623	1725±359	4209±557	0.12±0.03	12±4	1.0±0.2	Y	1548±225	3050±312	0.13±0.01	20±4
0731+4522	1778±107	3291±260	0.18±0.01	3.3±0.3	0.53±0.03	N	1885±134	3715±389	0.16±0.01	4.5±0.5
0735+3752	3120±303	4572±712	0.18±0.06	7±3	0.37±0.13	Y	3996±293	8070±838	0.14±0.06	7±4
0737+4244	1624±74	4326±133	0.22±0.01	3.8±0.2	0.41±0.02	N	1692±98	3361±148	0.19±0.01	6.2±0.5
0802+3104	2661±265	5707±652	0.10±0.02	34±7	2.0±0.4	Y	1772±185	4430±358	0.07±0.01	19.5±1.5
0811+1739	1779±66	4325±156	0.06±0.01	41±6	2.4±0.3	Y	1520±150	3520±253	0.11±0.02	31±9
0813+4608	1270±197	2992±471	0.08±0.08	5±7	0.3±0.3	Y	1430±91	2483±165	0.11±0.01	14.0±1.5
0831+0521	1040±328	1197±550	0.10±0.02	1.3±0.6	0.32±0.08	N	...	...	0.11±0.06	[0.06]
0845+3409	2090±294	3897±865	0.16±0.02	9.7±1.7	0.69±0.07	Y	1718±172	2820±310	0.16±0.02	7.5±1.2
0846+2522	2572±244	7398±410	0.09±0.02	20±3	1.04±0.14	Y	3394±402	8304±459	0.08±0.02	22±6
0847+1824	1665±193	3519±282	0.40±0.04	8.0±1.1	1.19±0.08	Y	...	...	0.27±0.11	[1.66]
0854+1741	2729±353	4642±602	0.16±0.02	5.67±1.08	0.84±0.11	Y	1472±269	2582±563	0.22±0.01	5±1
0857+0528	1959±193	4307±282	0.17±0.03	22±4	1.8±0.3	Y	1485±120	3499±51	0.1±0.01	17.0±1.3
0904+5536	2643±70	5724±125	0.26±0.02	7.8±0.4	0.48±0.03	Y	2483±36	7540±182	0.22±0.02	7.5±0.5
0909+1330	1721±251	4023±416	0.12±0.02	18±4	2.00±0.19	Y	1687±138	4418±148	0.19±0.04	45±8
0921+1017	2033±157	4900±498	0.23±0.04	4.6±0.9	0.31±0.05	Y	2317±286	4432±427	0.17±0.02	8.9±1.4
0923+2254	2195±254	3783±545	0.51±0.13	4.1±0.8	0.67±0.15	Y	1824±265	2924±668	0.24±0.03	9.4±2.0
0923+2946	2686±222	5946±522	0.13±0.02	5.9±1.1	0.24±0.03	Y	2936±247	5650±906	0.16±0.02	11.2±1.7
0927+2301	2624±226	7732±647	0.10±0.03	17±5	1.0±0.2	Y	2112±205	5377±367	0.08±0.01	17±2
0932+0233	2407±429	6863±625	0.13±0.01	10±2	0.50±0.04	Y	1814±72	4273±168	0.13±0.01	12.54±1.04
0932+0405	1829±75	5316±427	0.26±0.02	2.5±0.2	0.24±0.02	N	...	...	0.1±0.4	[0.41]
0936+1014	2259±153	4846±228	0.09±0.01	9.9±0.8	1.35±0.07	Y	1995±80	3916±123	0.10±0.01	17.02±1.07
0938+0743	1663±190	4813±684	0.14±0.02	11±2	1.04±0.12	N	3723±608	7110±808	0.15±0.12	4±4
0948+4030	1768±225	3460±258	0.17±0.05	12±4	1.2±0.4	Y	3188±438	6732±548	0.12±0.01	11.0±1.8
1002+2648	1944±184	5721±433	0.12±0.02	4.6±1.0	0.29±0.04	Y	...	...	0.12±0.04	[2.23]
1029+1408	2031±338	5264±381	0.14±0.02	9.8±2.0	0.80±0.08	Y	2456±344	6499±649	0.15±0.01	8.7±1.5
1029+2728	2103±233	4958±547	0.23±0.06	4.1±1.5	0.32±0.08	Y	1544±28	3634±152	0.25±0.03	5.07±1.06
1029+4019	2515±349	5985±401	0.11±0.02	8.4±1.5	0.64±0.07	Y	2193±387	5998±547	0.12±0.01	6.5±1.3
1038+4658	2621±322	4750±302	0.10±0.01	9.4±1.0	0.62±0.06	Y	...	...	0.10±0.14	[2.75]
1042+0414	1569±194	4064±166	0.34±0.03	6.6±1.0	0.57±0.04	Y	1518±102	2724±145	0.33±0.03	5.6±0.6
1043+1105	2864±149	6171±230	0.21±0.04	10.5±1.7	0.61±0.06	Y	2313±28	6597±152	0.13±0.01	4.7±0.2
1049+2451	2368±161	5181±207	0.15±0.03	14.2±1.8	0.97±0.14	Y	2534±135	5112±203	0.15±0.01	15.1±1.2
1058+5259	1987±400	4928±940	0.07±0.01	18±5	1.24±0.18	N	1896±150	5372±150	0.10±0.01	13.3±1.7
1101+1102	2558±125	6047±295	0.14±0.03	7.6±1.2	0.62±0.13	N	3949±170	8349±597	0.13±0.01	3.5±0.3
1104+4334	1873±308	4319±647	0.09±0.02	4.4±1.3	0.31±0.06	Y	1719±160	4072±395	0.12±0.01	9.4±1.2
1110+1136	1878±206	3860±400	0.14±0.01	10.4±1.6	0.78±0.05	Y	1378±95	2898±150	0.15±0.01	14.7±1.5
1116+4123	2531±294	6324±692	0.25±0.04	10.2±1.9	0.56±0.07	N	3136±315	6774±740	0.27±0.04	6.6±1.3
1118+2827	1908±136	5910±498	0.21±0.03	3.8±0.7	0.38±0.05	N	...	...	0.14±0.05	[2.05]
1132+1017	2028±147	5782±345	0.10±0.01	7.7±1.3	0.74±0.09	Y	1900±86	5341±740	0.09±0.01	15.8±1.4
1137+4826	1750±357	3663±647	0.34±0.05	5.8±1.4	0.94±0.14	Y	1606±92	3788±222	0.45±0.06	6.8±0.9
1139+5911	2333±158	4262±218	0.16±0.06	20±4	2.2±0.7	Y	2228±111	3994±221	0.09±0.01	22.2±1.7
1140+2307	2710±235	5014±668	0.10±0.01	8.0±1.2	0.43±0.05	N	3324±330	6376±586	0.12±0.01	4.4±0.6
1143+5941	2002±446	5629±863	0.13±0.04	15.0±2.7	0.77±0.18	Y	1790±128	5405±424	0.08±0.01	38±4
1144+3653	3016±292	8301±579	0.08±0.01	21±3	0.90±0.14	N	2933±205	8009±145	0.08±0.01	16.3±1.5
1145+5547	2078±422	4298±611	0.10±0.01	14±3	1.18±0.12	Y	1837±208	4465±391	0.15±0.01	7.49±1.06
1147+0902	3733±226	6475±563	0.14±0.05	13±3	0.9±0.3	N	2896±188	5285±543	0.12±0.01	10.9±1.2
1205+4959	3572±201	8275±650	0.11±0.02	3.9±0.4	0.24±0.03	Y	2678±294	5552±374	0.10±0.01	3.6±0.5
1206+4244	1925±167	3889±211	0.15±0.02	24±3	2.4±0.3	Y	1614±92	3800±144	0.17±0.02	36±3
1210+3820	2499±432	6413±513	0.20±0.04	5.9±1.5	0.36±0.06	N	2831±148	5300±392	0.20±0.02	8.0±0.7
1216+5049	3329±180	8923±422	0.11±0.02	2.3±0.3	0.19±0.03	Y	4487±477	7810±392	0.09±0.01	2.1±0.3
1223+0240	2780±160	5802±220	0.05±0.02	207±44	17±6	Y	2306±107	5051±168	0.10±0.01	69±6
1228+0951	2289±657	7303±1543	0.12±0.07	3±3	0.23±0.14	Y	2331±456	6011±495	0.12±0.04	3.2±1.6
1231+4504	1551±343	2872±440	0.20±0.03	5.5±1.4	1.27±0.14	Y	1555±168	3325±394	0.16±0.02	9.1±1.2
1241+3722	1829±93	4320±219	0.13±0.02	7.9±0.9	0.69±0.08	N	1574±100	3185±197	0.11±0.01	6.0±0.8
1246+5134	2402±313	4403±703	0.07±0.05	10±11	0.6±0.5	Y	1141±130	2270±185	0.09±0.01	12.0±1.8
1250-0249	2068±323	5304±732	0.17±0.03	9±2	0.89±0.13	Y	2417±246	5771±541	0.18±0.01	7.3±0.9
1306+4552	1327±148	3262±237	0.15±0.02	18±3	1.9±0.2	N	1892±297	4129±772	0.22±0.04	2.8±0.8
1307+0952	1616±114	3748±267	0.09±0.04	11±7	0.8±0.3	N	1630±165	3586±249	0.14±0.01	12.7±1.7
1312+2628	1585±171	3131±256	0.12±0.03	32±10	2.8±0.5	Y	1572±150	2924±345	0.22±0.03	36±6
1313+3653	2592±217	5591±402	0.14±0.02	4.8±0.5	0.34±0.03	Y	2115±264	4920±347	0.13±0.01	4.2±0.6

Table A2 — Continued

Object	$\sigma_{H\beta}$ SDSS [km s $^{-1}$ ]	$FWHM_{H\beta}$ SDSS [km s $^{-1}$ ]	$\frac{H\beta_{narrow}}{[OIII]}$ flux SDSS	$H\beta_{\frac{broad}{narrow}}$ flux SDSS	$H\beta_{\frac{broad}{narrow}}$ peak flux SDSS	FeII SDSS	$\sigma_{H\beta}$ Keck [km s $^{-1}$ ]	$FWHM_{H\beta}$ Keck [km s $^{-1}$ ]	$\frac{H\beta_{narrow}}{[OIII]}$ flux Keck	$H\beta_{\frac{broad}{narrow}}$ flux Keck
(1)	(2)	(3)	(4)	(5)	(6)	(7)	(8)	(9)	(10)	(11)
1323+2701	4266±349	10123±299	0.089±0.004	18.3±1.7	0.79±0.02	Y	2414±376	5219±782	0.10±0.01	5.9±1.2
1353+3951	2037±121	6308±537	0.19±0.02	4.1±0.5	0.31±0.02	N	...	...	0.2±0.7	[1.52]
1355+3834	2842±79	5936±245	0.28±0.05	3.3±0.3	0.36±0.06	Y	4034±301	6371±277	0.20±0.02	3.2±0.3
1405-0259	1873±212	3518±549	0.21±0.02	13±2	1.48±0.13	Y	1599±140	2933±260	0.16±0.02	11.1±1.4
1416+0317	11853±251	4022±589	0.12±0.02	5.4±1.1	0.78±0.09	Y	1514±233	3565±550	0.11±0.02	2.2±0.5
1419+0754	1940±154	5517±362	0.10±0.02	2.9±0.7	0.35±0.06	N	3006±371	5780±529	0.10±0.02	3.5±1.0
1423+2720	3428±264	7873±621	0.11±0.03	12±4	0.5±0.1	Y	...	...	0.08±0.04	[2.45]
1434+4839	2268±171	4351±534	0.08±0.02	35±7	2.7±0.6	Y	1731±85	4475±222	0.09±0.01	6.0±0.4
1505+0342	2280±215	5028±569	0.14±0.03	6.9±1.3	0.83±0.12	N	1956±139	5782±154	0.08±0.01	17.8±1.6
1535+5754	2431±311	4191±565	0.09±0.03	16±5	1.4±0.4	Y	2442±93	5088±127	0.08±0.01	16.2±1.3
1543+3631	1527±171	2849±197	0.14±0.02	7.1±1.1	1.03±0.15	Y	1820±168	3831±248	0.09±0.01	4.0±0.5
1545+1709	2158±156	5555±275	0.09±0.01	6.5±0.6	0.52±0.05	N	3588±226	4612±237	0.06±0.01	24±3
1554+3238	2067±104	4887±246	0.14±0.02	7.2±0.8	0.83±0.11	N	2523±159	4148±258	0.11±0.01	7.9±0.7
1557+0830	13174±214	5054±185	0.18±0.03	11.9±1.5	0.87±0.09	Y	2388±91	4817±156	0.17±0.02	15.1±1.4
1605+3305	2153±101	5079±230	0.06±0.02	54±13	2.9±1.0	Y	1960±272	5302±637	0.10±0.01	33±5
1606+3324	2158±170	5087±393	0.10±0.01	3.8±0.5	0.34±0.04	N	2053±80	5088±739	0.12±0.01	4.4±0.3
1611+5211	1392±207	3895±486	0.16±0.03	4.8±1.1	0.71±0.10	N	2515±410	7695±964	0.12±0.03	2.9±1.1
1636+4202	2367±223	6655±621	0.07±0.01	39±7	3.7±0.4	Y	2492±230	4542±523	0.10±0.01	24±3
1647+4442	2227±279	6228±655	0.09±0.02	4.8±1.9	1.3±0.4	N	2921±246	8325±214	0.20±0.03	21±4
1655+2014	...	...	...	...	...	N	...	...	...	...
1708+2153	2829±134	6055±580	0.11±0.01	15.2±1.2	1.49±0.08	Y	2402±122	7359±245	0.13±0.02	62±10
2116+1102	2790±27	6577±64	0.0903±0.0002	2.25±0.02	0.1831±0.0003	Y	2484±42	7186±248	0.084±0.005	3.63±0.18
2140+0025	1329±104	2225±127	0.53±0.09	7.1±1.1	1.47±0.12	Y	1114±64	2155±127	0.29±0.04	17±2
2215-0036	1877±200	3330±155	0.12±0.01	8.5±1.1	1.58±0.14	Y	1636±92	3966±220	0.09±0.01	7.3±0.6
2221-0906	2498±394	6684±539	0.10±0.01	21±4	1.20±0.10	N	2375±131	6012±224	0.12±0.01	24±2
2222-0819	1811±88	3327±319	0.25±0.02	2.5±0.2	0.55±0.03	N	1799±168	2861±343	0.2±0.02	2.5±0.3
2233+1312	1897±66	4409±236	0.19±0.02	6.7±0.4	0.90±0.06	N	2477±135	5830±318	0.16±0.01	5.7±0.5
2254+0046	1466±200	2015±195	0.56±0.09	3.9±0.8	1.26±0.17	Y	859±194	1398±286	0.59±0.07	4.7±1.1
2327+1524	3267±206	4098±707	0.06±0.01	11.0±1.6	1.10±0.13	N	1924±166	5807±390	0.08±0.02	2.0±0.7
2351+1552	3533±269	10437±526	0.12±0.01	3.6±0.4	0.20±0.02	N	2974±144	7803±394	0.11±0.01	6.7±0.6

Note. — Col. (1): Target ID based on R.A. and Dec. used throughout the text. Col. (2): Second moment of broad H $\beta$  from SDSS spectrum (in km s $^{-1}$ ). Col. (3): Full-width at half-maximum of broad H $\beta$  from SDSS spectrum (in km s $^{-1}$ ). Col. (4): Integrated flux ratio of H $\beta$ /[OIII] from SDSS spectrum. Col. (5): Integrated flux ratio of H $\beta$  broad/narrow from SDSS spectrum. Col. (6): Peak flux ratio of H $\beta$  broad/narrow from SDSS spectrum. Col. (7): Whether or not FeII was subtracted from the SDSS spectrum during the fitting process. Col. (8): Second moment of broad H $\beta$  from Keck spectrum (in km s $^{-1}$ ). Col. (9): Full-width at half-maximum of broad H $\beta$  from Keck spectrum (in km s $^{-1}$ ). Col. (10): Integrated flux ratio of H $\beta$ /[OIII] from Keck spectrum. Col. (11): Integrated flux ratio of H $\beta$  broad/narrow from Keck spectrum. Col. (12): Peak flux ratio of H $\beta$  broad/narrow from Keck spectrum. Col. (13): Whether or not FeII was subtracted from the Keck spectrum during the fitting process.

Note that values in brackets are estimated from upper limits on the broad H $\beta$  flux for objects classified as Sy 1.9 or Sy 2, that is without an obvious broad H $\beta$  component. No width (FWHM or  $\sigma$ ) of broad H $\beta$  is given in those cases. Also note that for object 1655+2014 the signal-to-noise ratio was too low in both SDSS and Keck spectra to produce a reliable fit to the H $\beta$  region. No values are given for this object and it is not included in the quantitative analysis.

## B. SDSS VS. KECK SPECTRA COMPARISON

## C. FITS TO SDSS AND KECK SPECTRA

## REFERENCES

- Adelman-McCarthy, J. K., Agueros, M. A., Allam, S. S., et al. 2008, *ApJ*, 175, 297  
Antonucci, R. R. J. & Cohen, R. D. 1983, *ApJ*, 271, 564  
Arcavi, I., Gal-Yam, A., Sullivan, M., et al. 2014, *ApJ*, 793, 38  
Aretxaga, I., Joguett, B., Kunth, D., Melnick, J., & Terlevich, R. J. 1999, *ApJ*, 519, L123  
Barth, A. J., Bennert, V. N., Canalizo, G., et al. 2015, *ApJS*, 217, 26  
Bennert, V. N., Auger, M. W., Treu, T., Woo, J. H., Malkan, M. A. 2011, *ApJ*, 726, 59  
Bennert, V. N., Treu, T., Auger, M. W., et al. 2015, *ApJ*, 809, 20  
Bentz, M. C., Denney, K. D., Cackett, E. M., et al. 2007, *ApJ*, 662, 205  
Bentz, M. C., Denney, K. D., Grier, C. J., et al. 2013, *ApJ*, 767, 149  
Bochkarev, N. G., 2006, *ASPC*, 360, 285  
Boroson, T. A., & Green, R. F. 1992, *ApJS*, 80, 109  
Denney, K. D., Peterson, B. M., Dietrich, M., Vestergaard, M. & Bentz, M. C. 2009, *ApJ*, 692, 246  
Denney, K. D., Rosa, G. D., Croxall, K., et al. 2014, *ApJ*, 796, 134  
Dimitrijević, M. S., Popović, L. Ć., Kovačević, J., Dačić, M., & Ilić, D. 2007, *MNRAS*, 374, 1181  
Drake, A. J., Djorgovski, S. G., Mahabal, A., et al. 2009, *ApJ*, 696, 870  
Elitzur, M., Ho, L. C., & Trump, J. R. 2014, *MNRAS*, 438, 3340  
Eracleous, M., & Halpern, J. P. 2001, *ApJ*, 554, 240  
Ferrarese, L., & Merrit, D. 2000, *ApJ*, 539, L9  
Filippenko, A. V. 1997, *ARA&A*, 35, 309  
Gebhardt, K., Bender, R., Bower, G., et al. 2000, *ApJ*, 539, L13  
Goad, M. R. & Korista, K. T. 2014, *MNRAS*, 444, 43  
Goodrich, R. W., 1989, *ApJ*, 340, 190  
Graham, A. 2016, *Galactic Bulges, Astrophysics and Space Science Library*, Volume 418, E. Laurikainen, R.F. Peletier, and D.A. Gadotti (eds.), Springer Publishing  
Harris, C. E., Bennert, V. N., Auger, M. W., et al. 2012, *ApJS*, 201, 29  
Hicks, E. K. S., & Malkan, M. A. 2008, *ApJS*, 174, 31  
Ho, L. C., & Kim, M. 2009, *ApJS*, 184, 398  
Kaspi, S., Maoz, D., Netzer, H., et al. 2005, *ApJ*, 629, 61  
Kollatschny, W. & Fricke, K. J., 1985, *A&A*, 146, L11  
Komossa, S., 2012, *Advances in Astronomy*, Vol. 2012, id. 364973

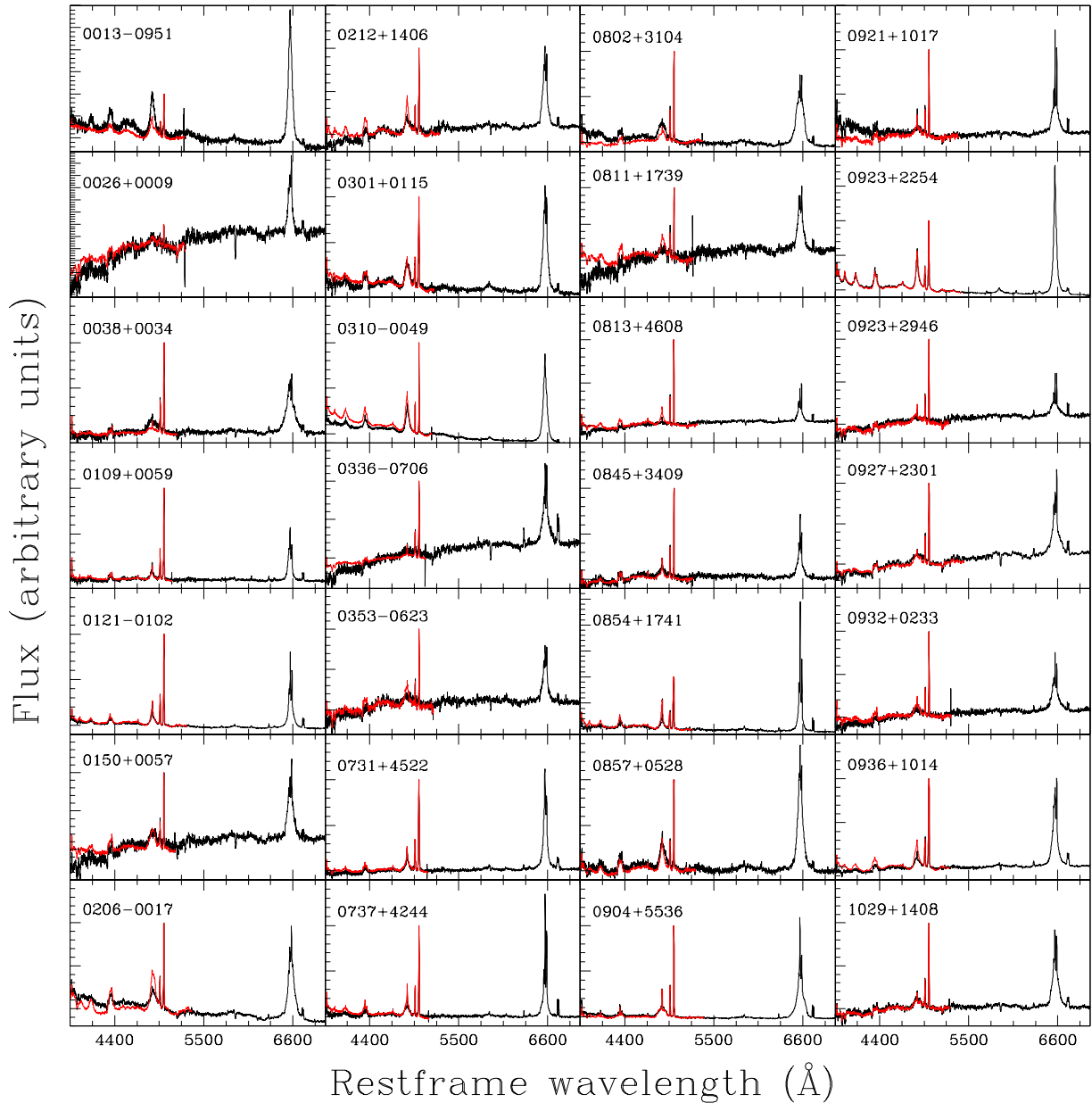


**Figure B1.** Unabsorbed spectra comparing SDSS (black) and Keck (red) (3850-7000Å). Note that the Keck spectra only cover the blue part. For comparison, the base of the 5007Å [OIII] line is set to 0 and the peak to 1 to make the data sets comparable as discussed in the text. Objects shown in this figure are included in [Bennert et al. \(2015\)](#).

- Komossa, S., Zhou, H., Wang, T., et al., 2008, *ApJ*, 678, L13  
 Korista, K. T. & Goad, M. R. 2004, *ApJ*, 606, 749  
 Kormendy, J., & Ho, L. C. 2013, *ARAA*, 51, 511  
 Kormendy, J., & Richstone D. 1995, *ARA&A*, 33, 581  
 Kovacevic J., Popovic L.C., Dimitrijevic M.S. 2010, *ApJS*, 189, 15  
 LaMassa, S. M., Cales, S., Moran, E. C., et al. 2015, *ApJ*, 800, 144  
 Leighly, K. M., Cooper, E., Grupe, D., et al., 2015, *ApJ*, 809, L13  
 Lyutyi, V. M., Oknyanskii, V. L., & Chuvaev, K. K. 1984, *SvAL*, 10, 335  
 MacLeod, C. L., Ross, N. P., Lawrence, A. et al. 2015, *ApJ*, submitted (arXiv:1509.08393)  
 Magorrian, J., Tremaine, S., Richstone, D. et al. 1998, *AJ*, 115, 2285  
 McGill, K. L., Woo, J. H., Treu, T., & Malkan, M. A. 2008, *ApJ*, 673, 703  
 Merloni, A., Dwelly, T., Salvato, M., et al. 2015, *MNRAS*, 452, 69  
 Nicastro, F., 2000, *ApJ*, 530, L65  
 Osterbrock, D. E. 1977, *ApJ*, 215, 733  
 Osterbrock, D. E. 1981, *ApJ*, 249, 462

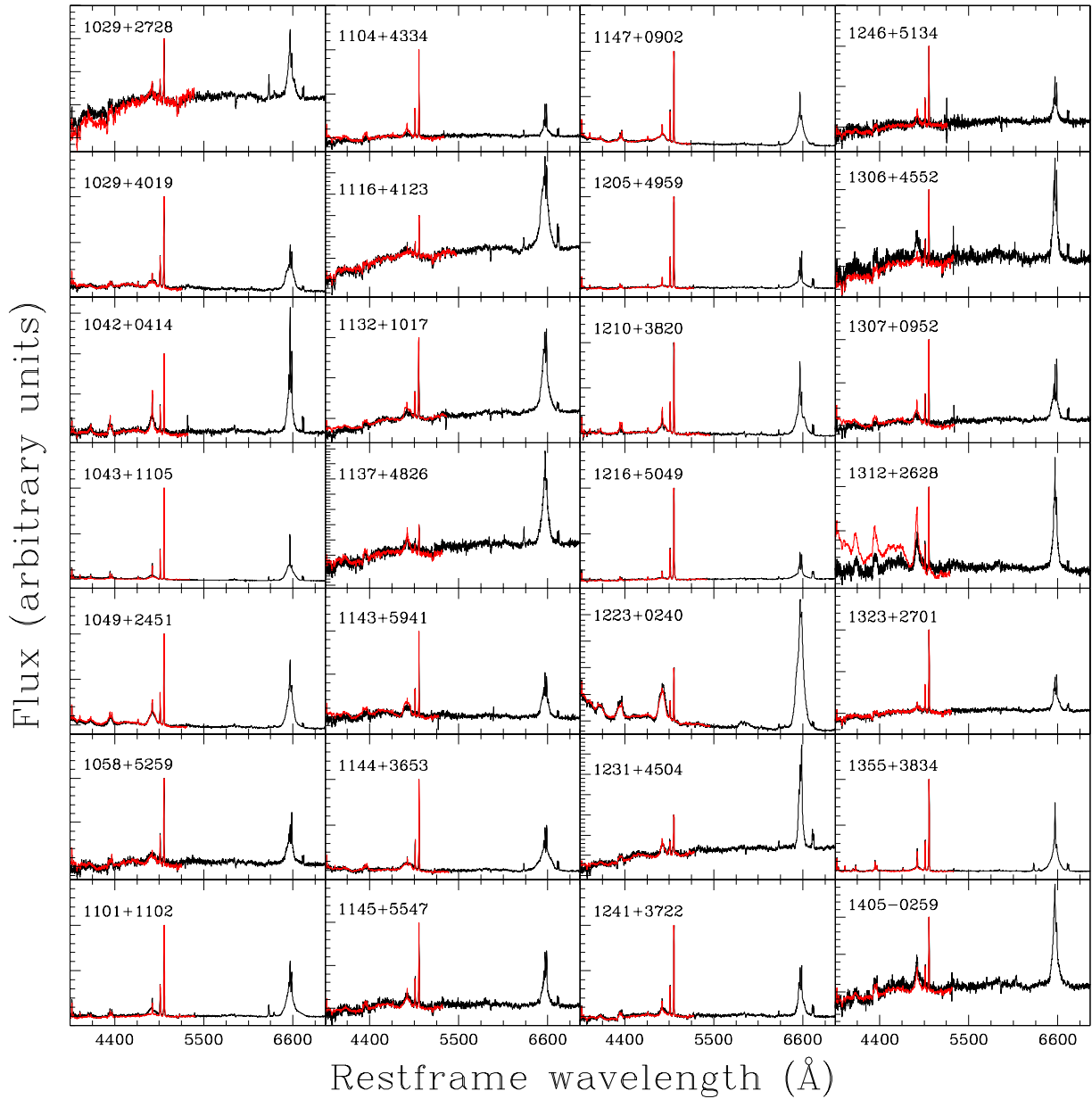
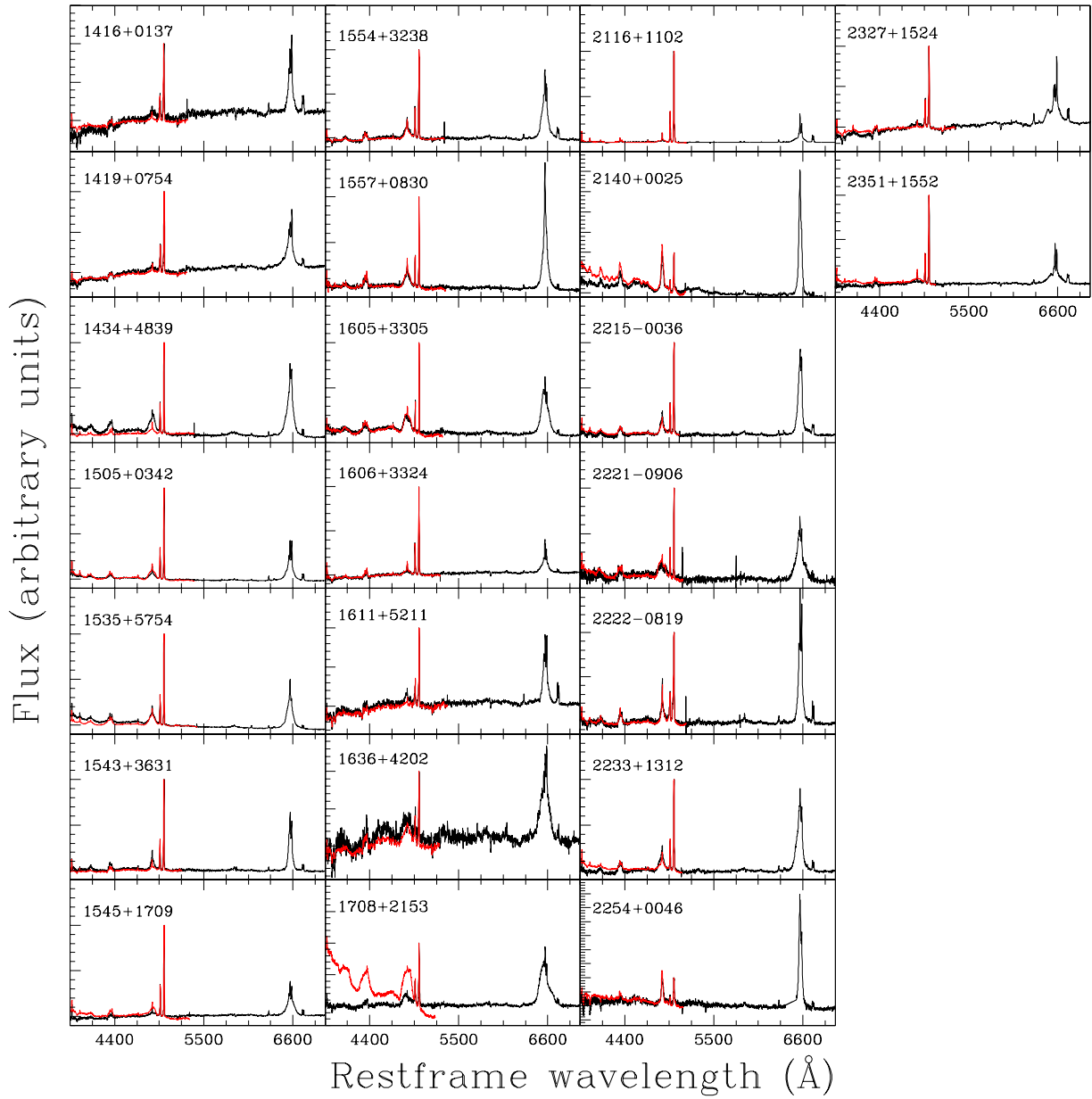


Figure B2. Same as Figure B1.

- Osterbrock, D. E. 1989, *Astrophysics of Gaseous Nebulae and Active Galactic Nuclei* (University Science Books: Mill Valley)
- Osterbrock, D.E., & Koski, A.T. 1976, MNRAS, 176, 61
- Pancoast, A., Brewer, B. J., Treu, T., et al. 2014, MNRAS, 445, 3073
- Park, D., Woo, J. H., Treu, T., et al. 2012 ApJ, 747, 30
- Park, D., Woo, J. H., Bennert, V. N., et al. 2015, ApJ, 799, 164
- Parker, M. L., Fabian, A. C., Matt, G., et al., 2015, MNRAS, 447, 72
- Penston, M. V. & Perez, E. 1984, MNRAS, 211, 33
- Peterson, B., Denney, K. D., De Rosa, G., et al. 2013, 779, 2
- Rees, M.J., 1988, Nature, 333, 523
- Rosenblatt, E. I., Malkan, M. A., Sargent, W. L. W., & Readhead, A. C. S. 1994, ApJS, 93, 73
- Ruan, J. J., Anderson, S. F., Cales, S. L. et al., 2015, ApJ, submitted (arXiv:1509.03634)
- Runnoe, J. C., Cales, S., Ruan, J. F. et al., 2016, MNRAS, 455, 1691
- Scott, B. 2013, Time Variation of the Broad H $\beta$  and H $\alpha$  Emission Lines in Active Galactic Nuclei, Cal Poly Digital Commons
- Shapovalova, A. I., Popovic, L. C., & Burenkov, A. N. et al. 2010, A&A, 509, A106
- Shappee, B. J., Prieto, J. L., Grupe, D., et al. 2014, ApJ, 788, 48
- Shen, J., Vanden Berk, D. E., Schneider, D. P., Hall, P. B. 2008, ApJ, 135, 928
- Shen, Y., Richards, G. T., Strauss, M. A., et al. 2011, ApJS, 194, 45



**Figure B3.** Same as Figure B1.

Sperhake, U., 2015, *Astrophysics & Space Science Proceedings*, 40, 185  
 Storchi-Bergmann, T., Baldwin, J. A., & Wilson, A. S. 1993, *ApJ*, 410, L11  
 Tohline, J. E., & Osterbrock, D. E. 1976, *ApJ*, 210, L117  
 Trippe, M. L., Crenshaw, D. M., Deo, R., & Dietrich, M. 2008, *AJ*, 135, 2048  
 Valdez, F., Gupta, R., Rose, J. A., Singh, H. P., & Bell, D. J. 2004, *ApJS*, 152, 251  
 van der Marel, R. P. & Franx, M. 1993 *ApJ*, 407, 525  
 van der Marel, R. P., Cretton, N., de Zeeuw, P. T., & Rix, H. 1998, *ApJ*, 493, 613  
 Wandel, A., Peterson, B. M., & Malkan, M. A. 1999, *ApJ*, 526, 579  
 Woo, J. H., Treu, T., Malkan, M. A., & Blanford, R. D. 2006 *ApJ*, 645, 900

D. SDSS MULTI-COLOR IMAGES FOR 0847+1824 & 1038+4658



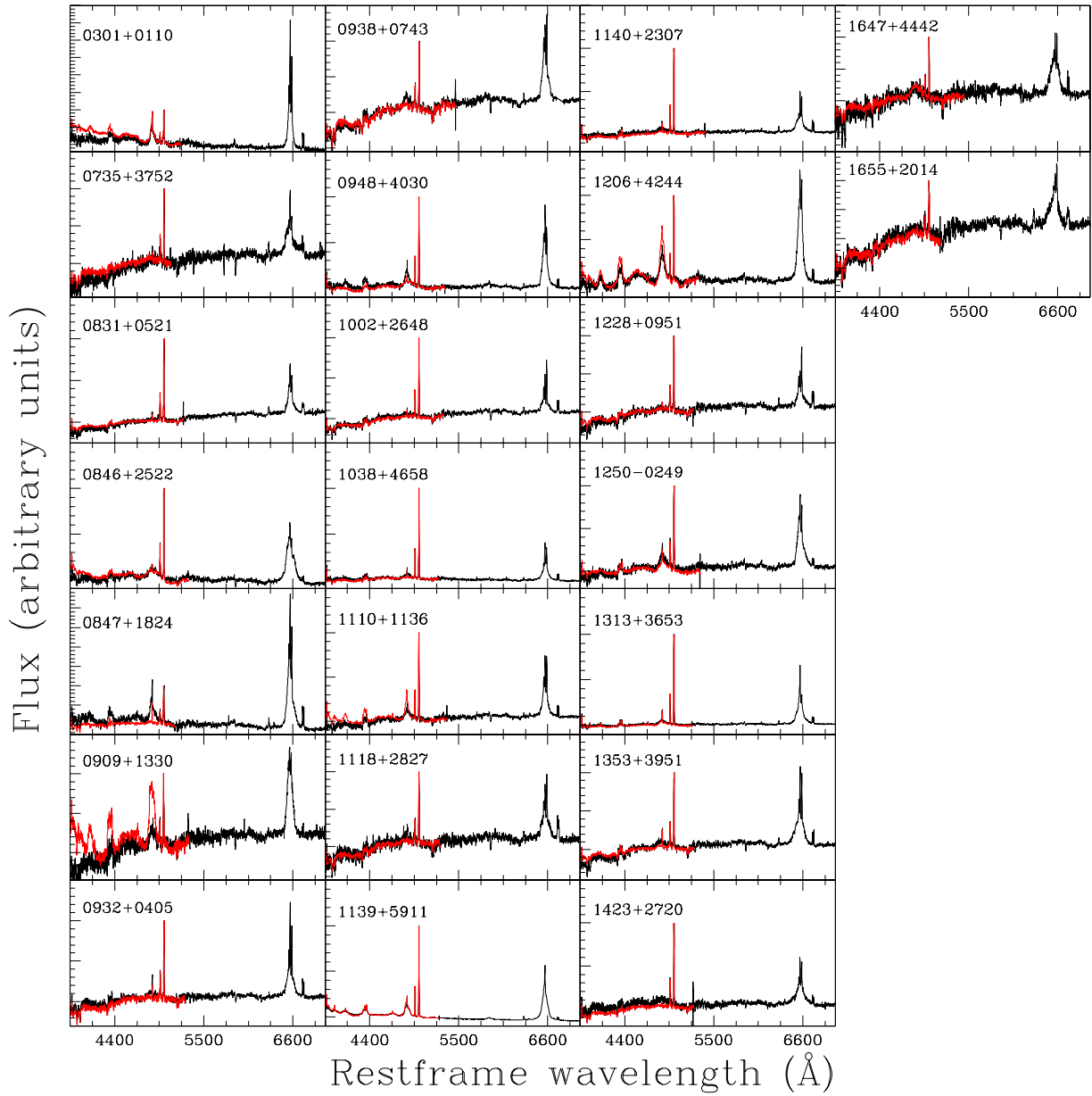
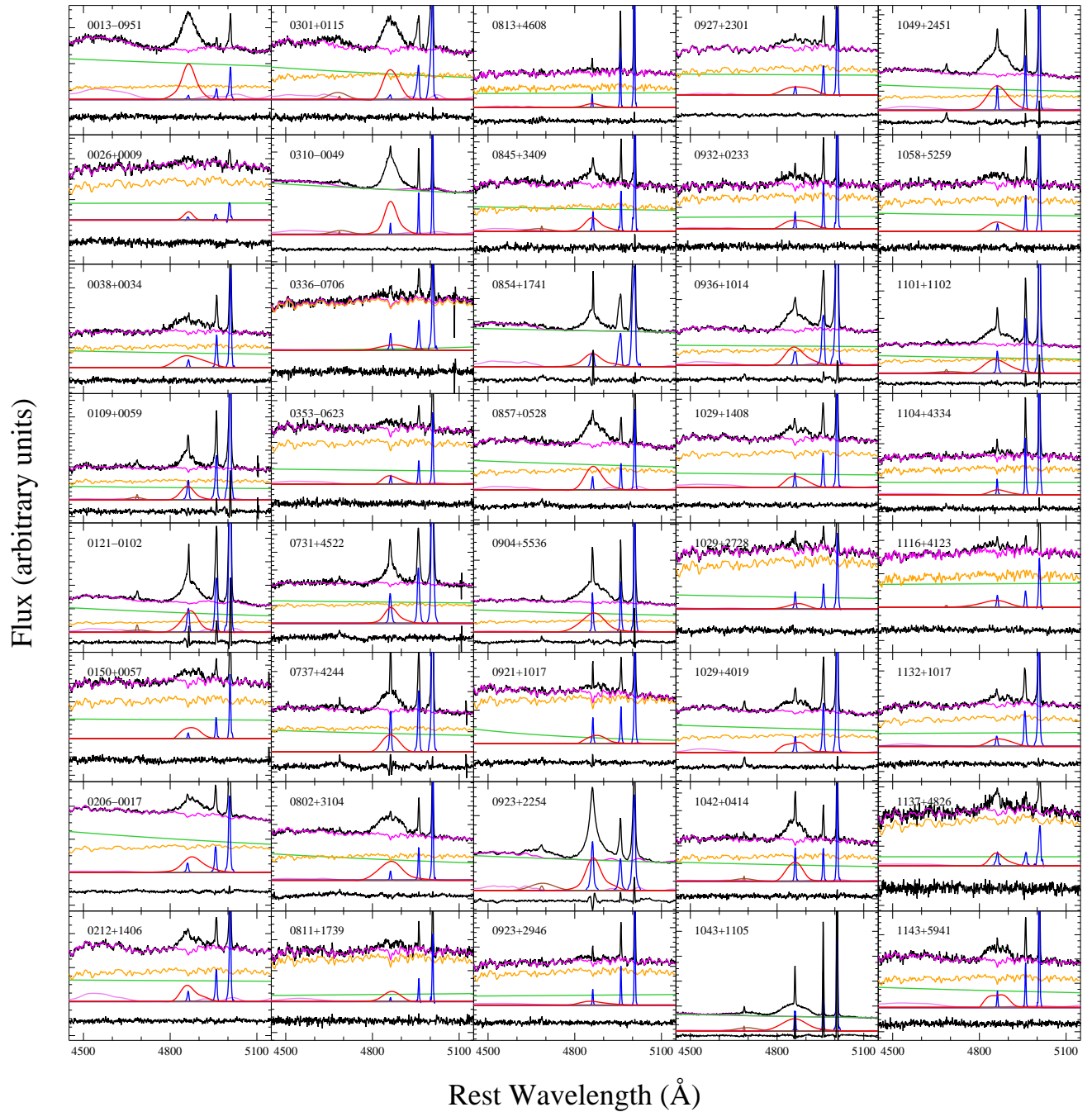


Figure B4. Same as Figure B1, except that these are the 23 objects not included in [Bennert et al. \(2015\)](#).



**Figure C1.** Multi-component spectral decomposition of the H $\beta$  region in SDSS spectra. In the upper region, the observed spectrum is shown in black with the best-fit of the continuum, FeII, and host galaxy starlight in magenta. Below that the best-fit to the power-law continuum is shown in green with the stellar spectrum in yellow. Below this, the narrow lines of H $\beta$  $\lambda$ 4861, and [OIII] $\lambda\lambda$ 4959,5007 are shown in blue, the broad and narrow components of HeII  $\lambda$ 4686 in brown, and the broad component of H $\beta$  in red. The residuals are plotted in black (arbitrarily shifted downward for clarity). Note that the objects shown here are included in [Bennert et al. \(2015\)](#) who show the corresponding fit to the Keck spectra in their Figure 3.

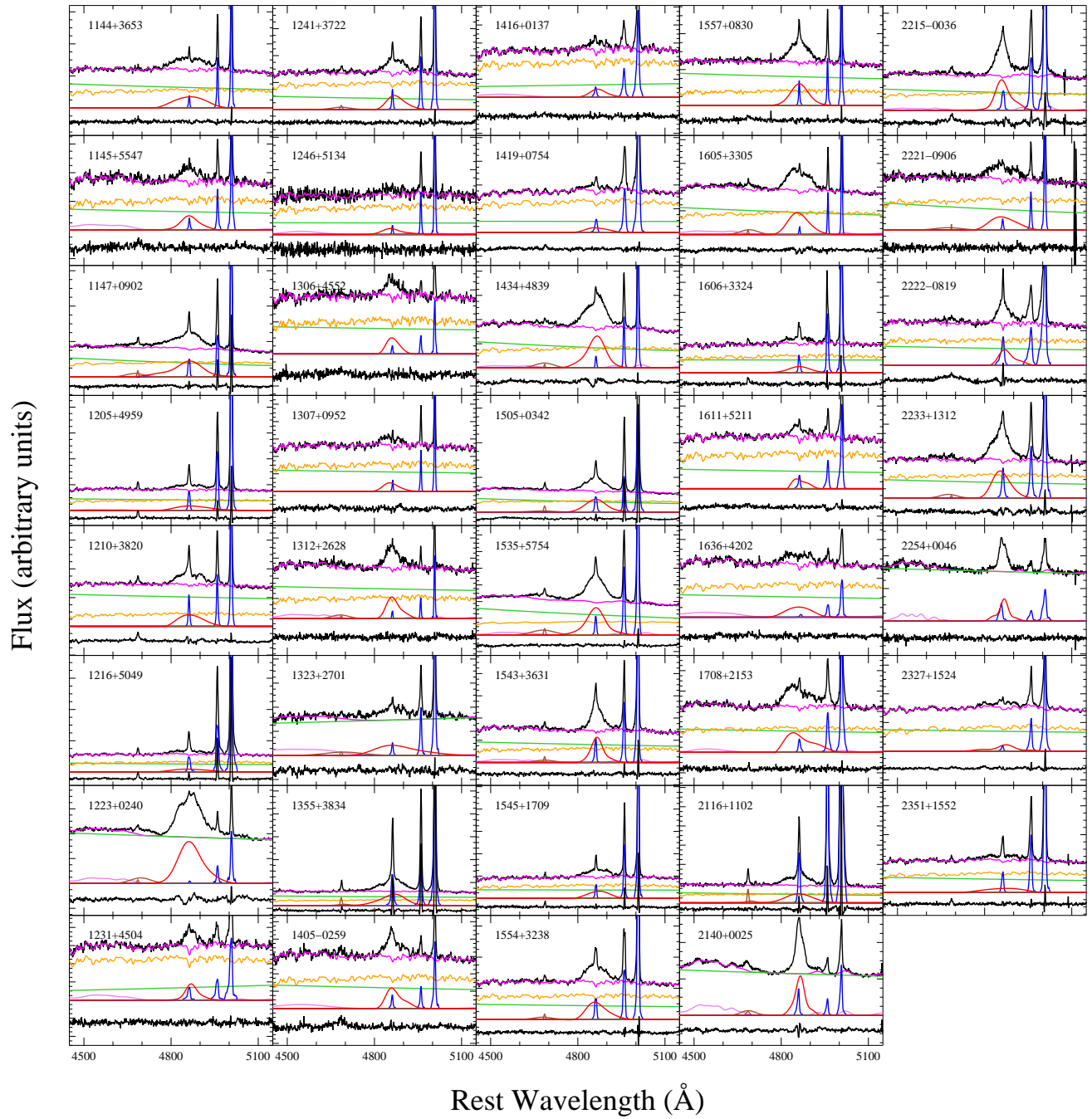


Figure C2. Same as Figure C1.

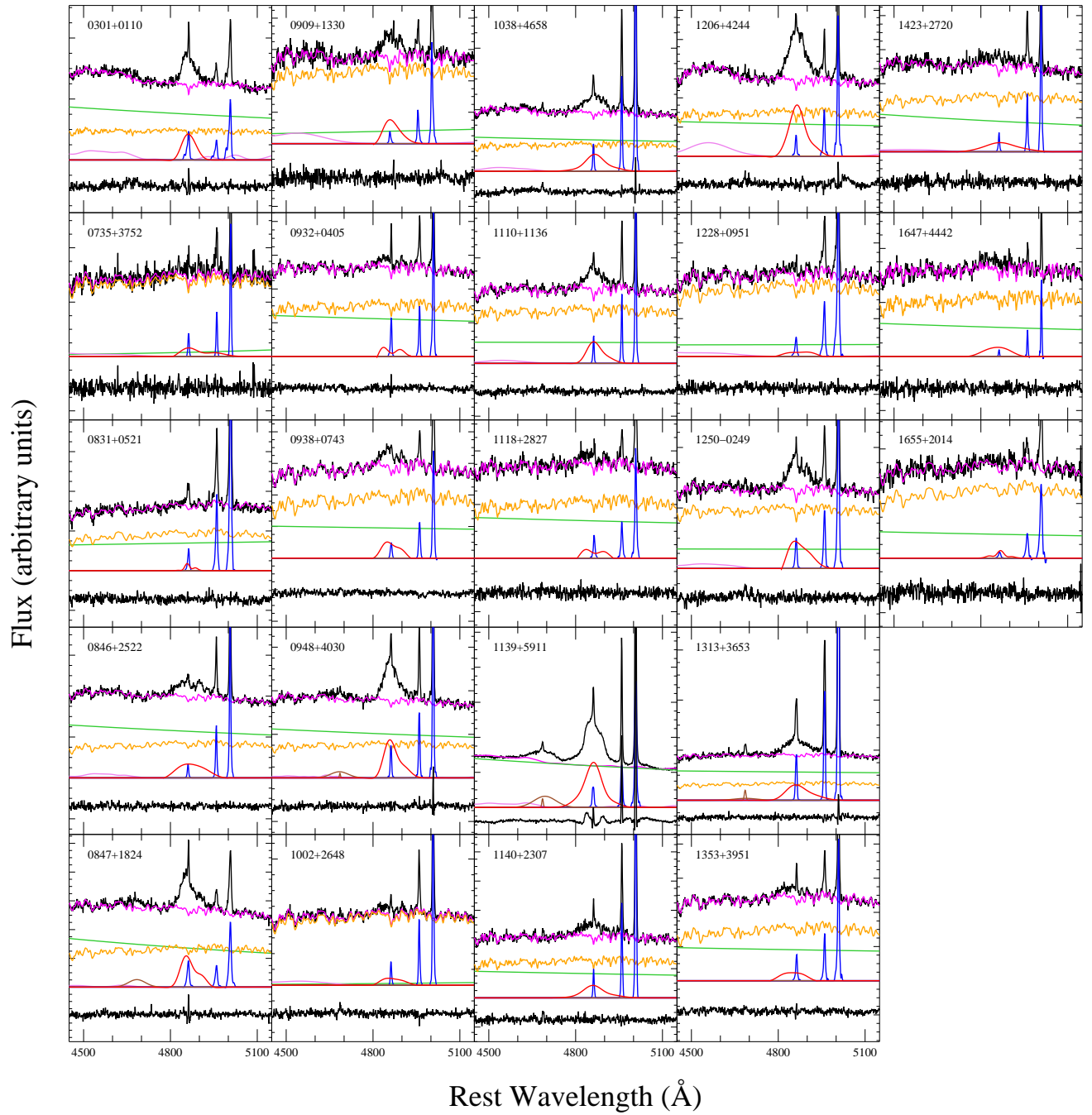


Figure C3. Same as Figure C1, but for 23 objects not included in [Bennert et al. \(2015\)](#).

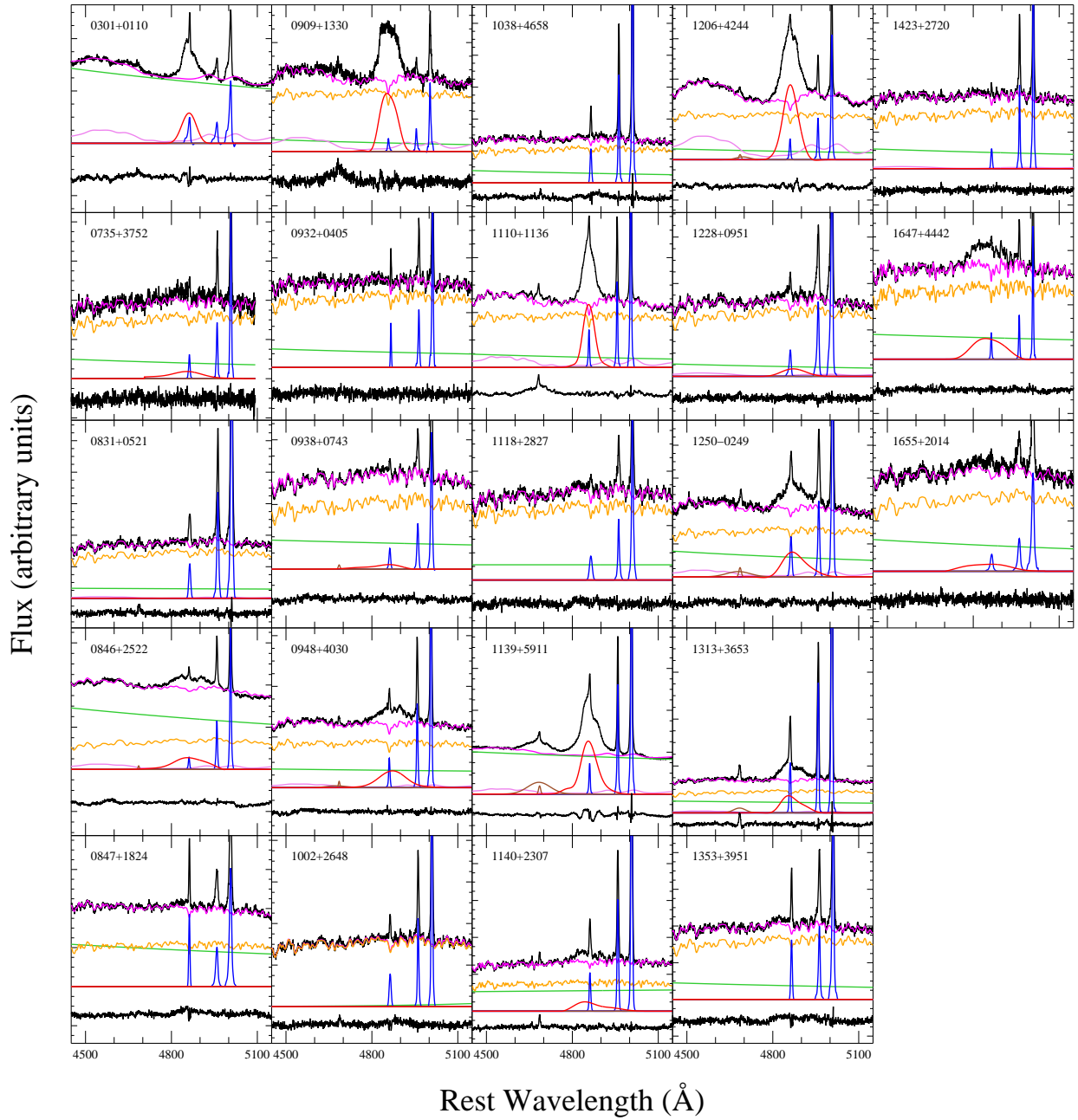
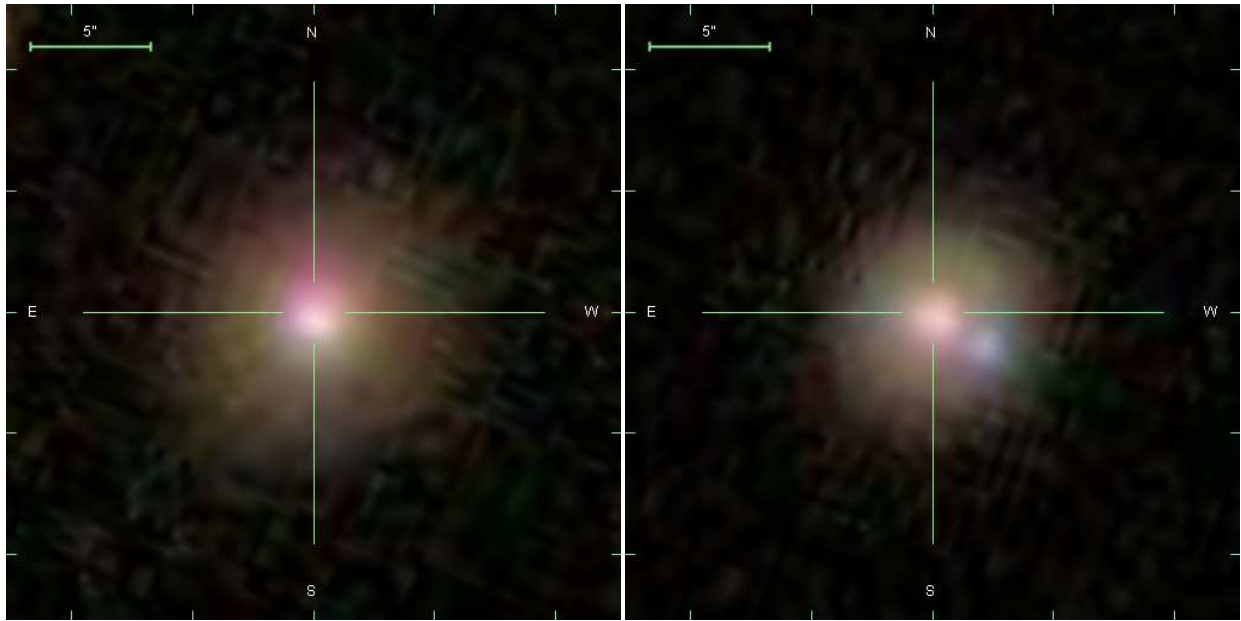


Figure C4. Same as Figure C3 for spectra gathered from Keck and not included in [Bennert et al. \(2015\)](#).



**Figure D1.** SDSS multi-color image for 0847+1824 (left; taken roughly a year before the SDSS spectrum, on 12-13-2004) and 1038+4658 (right; taken roughly 10 months before the SDSS spectrum, on 02-08-2002). For 0847+1824, there is extended emission offset  $\sim 1''$  to the north-east of the galaxy center. For 1038+4658, an emission blob can be seen  $\sim 2.5''$  to the south-west of the galaxy center. In both cases, the extended emission might have been missed in the Keck spectra due to the smaller width longslit (with a position angle not covering the emission), but included in the  $3''$  fiber of SDSS.